Post Access Report

Two-Stage Ocean Current Turbine Modeling: Computational Fluid Dynamics Informed Reduced-Order Model for Future Optimization

Awardee: Equinox Ocean Turbines

Awardee point of contact: Pieter de Haas

Facility: National Laboratory of the Rockies

Facility point of contact: Will Wiley

Date: March 26, 2026

TEAMER
Testing & Expertise for Marine Energy

EXECUTIVE SUMMARY

The Equinox Ocean Turbines (EQOT) current energy converter has a unique design with power generation in two small-diameter turbines attached to the tips of a large-diameter passive rotor. This configuration offers some key advantages for capturing ocean currents. With no centrally placed generator, almost no reaction torque is required at the nacelle of the main large-diameter rotor, and the small-diameter tip turbine generators operate at a higher speed and lower torque. The physics that determine the performance and loads on the turbine are also unique. The interactions of the flow field between the two stages and the general architecture of the system cannot be captured with traditional mid-fidelity modeling tools. For design iterations and large sets of load cases, it is important to have mid-fidelity models that can capture the important phenomenon with enough accuracy to identify global trends. This work uses a limited set of high-fidelity computational fluid dynamics (CFD) simulations to help inform the selection of and construction of a custom mid-fidelity model. Mid-fidelity modeling approaches were verified by comparing key turbine performance quantities to those found with the CFD model.

Hydrodynamic interactions of the two-stage rotor were identified through high-fidelity CFD modeling. This highlighted the impact of the main rotor tip vortex and wake on the secondary rotor apparent inflow. This results in a relative flow rotation and sharp deficit, that change the optimal secondary rotor rotation speed and adds unsteadiness to the blade loading respectively. Multiple mid-fidelity approaches were evaluated for their ability to capture these effects. A simple approximation of the combined-stage performance based on single-stage BEM provides a reasonable rough prediction, especially near the peak TSR values, with some larger discrepancy at higher TSRs. Predicting the combined-stage performance based on single-stage CFD data improves this prediction across the TSR range. Although the combined-stage modeling in OLAF was not successful in this stage of the project, it showed promise as a mid-fidelity method, assuming the parameters can be tuned to account for the significant differences in time and length scales between the main and secondary rotors. This may be addressed through code changes in future work. A significant finding from the OLAF work was the agreement between the vortex core radius values found independently via a parameter space search and via CFD. The technique of using single-stage secondary rotor BEM, with a custom inflow taken from single-stage main rotor CFD or OLAF, provides an efficient method to capture one-way coupled flow interactions. This method provided generally good predictions of the impact of the flow rotation on the secondary rotor but struggled to accurately predict the peaks of the unsteady load progression. Future work could include some superposition of a tuned main rotor trailing edge viscous wake into the custom inflow to better predict this interaction.

The next step is to look at the full semi-floating system. A number of additions are needed, including:

- Six-degree-of-freedom platform motions
- Non-fixed rotor speeds
- Moorings
- Non-uniform inflow

This full system modeling will be the subject of future proposals.

1 INTRODUCTION TO THE PROJECT

The Equinox Ocean Turbines (EQOT) current energy converter has a unique design with power generation in two small-diameter turbines attached to the tips of a large-diameter passive rotor. This configuration offers some key advantages for capturing ocean currents. With no centrally placed generator, almost no reaction torque is required at the nacelle of the main large-diameter rotor, and the small-diameter tip turbine generators operate at a higher speed and lower torque. The physics that determine the performance and loads on the turbine are also unique. The interactions of the flow field between the two stages and the general architecture of the system cannot be captured with traditional mid-fidelity modeling tools. For design iterations and large sets of load cases, it is important to have mid-fidelity models that can capture the important phenomenon with enough accuracy to identify global trends. This work uses a limited set of high-fidelity computational fluid dynamics (CFD) simulations to help inform the selection of and construction of a custom mid-fidelity model. The final model will be verified by comparing key turbine performance quantities to those found with the CFD model.

2 ROLES AND RESPONSIBILITIES OF PROJECT PARTICIPANTS

National Laboratory of the Rockies (NLR) and EQOT plan to meet two times a month to discuss project progress and action items. This frequency can be adjusted based on availability. Both groups will work together to select the best mid-fidelity strategy based on the results of the initial CFD and based on each group's unique experience and insight.

2.1 APPLICANT RESPONSIBILITIES AND TASKS PERFORMED

EQOT will provide the baseline system definition, including the following information:

- Foil section properties for both the main rotor and the tip turbine rotors
- Mass and inertia properties for turbine components
- Expected range of operating rotation speeds for each stage based on previously completed analyses
- Expected range of inflow velocities
- Other properties for setting up the mid-fidelity models, as needed

EQOT will provide insights into important operating conditions and flow effects.

2.2 NETWORK FACILITY RESPONSIBILITIES AND TASKS PERFORMED

NLR will perform the numerical analysis described in further detail in Section 6 and provide insights from their marine turbine modeling experience and code development.

The work includes setting up and running the initial blade-resolved CFD. Some check of spatial and temporal discretization convergence will be performed. NLR will also perform the post-processing of these high-fidelity loads.

After both groups select the best mid-fidelity strategy based on the CFD results, NLR will set up and implement the chosen model. NLR will run all load cases on the NLR high-performance computer (HPC). NLR will perform the post-processing of the mid-fidelity loads and make verification comparisons to the relevant CFD results.

3 Project Objectives

Mid-fidelity modeling tools are necessary for design iterations and optimization and for modeling a large set of possible environmental condition load cases. Existing mid-fidelity modeling tools cannot be immediately used for analysis of the unique tip turbine design. The first objective is to identify what type of mid-fidelity strategy could be the most effective, based on identified flow effects observed in high-fidelity CFD results. Flow interactions between the main rotor and the tip turbine rotors will be of particular interest.

The second objective is to effectively modify existing mid-fidelity tools to model the EQOT system. The model will be used to run a range of load cases and will be transferred to EQOT at the end of the project for further load case exploration and future design improvements.

The third objective is to verify the efficacy of the model by comparing key performance parameters to those found with CFD. These parameters include power, thrust, and rotation speed for the tip turbines and the system as a whole. The discrepancies in these values between the mid-fidelity model and the CFD will determine the effectiveness of the resulting model.

4 Test Facility, Equipment, Software, and Technical Expertise

NLR has extensive experience in turbine modeling, and numerous open-source tools developed by NLR for wind turbines are being adapted for marine turbines. One such tool is OpenFAST, an aero-hydro-elastic engineering model for whole turbines. Due to the novelty of the design, individual OpenFAST modules will need to be coupled using a new wrapper code. This work requires extensive knowledge of the OpenFAST code base and capabilities. The NLR team also has significant experience with CFD modeling of marine turbines, and a large computational resource. The CFD will be performed using the commercial code STAR-CCM+ on the NLR HPC. The NLR marine turbine modeling team has access to a STAR-CCM+ license.

5 Test or Analysis Article Description

The EQOT ocean current turbine, shown in Figure 1, consists of a large, central, two-bladed rotor with smaller turbines attached at the tips of each of the larger blades. The central rotor contains only a bearing and produces no power. All energy generation comes from the two tip turbines, which spin at a much higher rate than the central rotor. The tip turbines are fixed to the trailing edge of the main rotor, operating in a downstream manner with respect to the relative inflow. The full-scale device is semi-floating, meaning that it is submerged in the middle of the water column. One primary advantage of this

design is the elimination of significant moments about the main rotor. This enables the turbine to utilize only a simple, single-point mooring, reducing costs and enabling deployment in deep water. A traditional turbine with this mooring configuration would have minimal resistance to the rotor torque, making power generation impossible. A second advantage is elimination of a large central generator. The smaller turbines operate at a higher speed and lower torque, reducing the size and expense of the power take-off system.

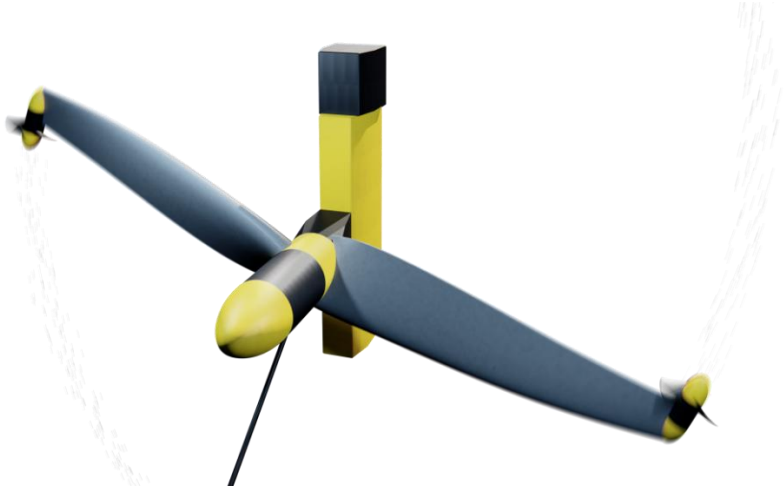

Figure 1. EQOT 50-meter tip turbine current energy converter. Source: https://equinoxoceanturbines.com/

The resulting model from this work will allow the EQOT team to make further improvements to the design of the turbine with greater confidence in the accuracy of load predictions.

6 Work Plan

6.1 Numerical Model Description

Figure 2 gives an overview of the planned workflow for the project. The project will involve a combination of high-fidelity CFD simulations and mid-fidelity simulations, either using a free vortex wake (FVW) method or a blade element momentum (BEM) method. The CFD portion will use the commercial code, STAR-CCM+, developed and maintained by Siemens. The mid-fidelity portion will use modules of the open-source code, OpenFAST, developed and maintained by NLR (NLR, GitHub OpenFAST, 2025). Selection of the mid-fidelity model (FVW or BEM) will depend on the results from the initial CFD simulations. Only one of the two lower branches in the flow chart will be performed. Both the FVW and BEM methods are within the AeroDyn module of OpenFAST. The name of the FVW method within AeroDyn is OLAF. The OpenFAST modules for structural motions (ElastoDyn), controls (ServoDyn), and additional structural forces (StC) will also be used. Both mid-fidelity approaches will require a custom wrapper developed in this project.

The first small set of CFD runs will provide insight into the specific flow patterns that need to be captured to model this unique device. Next, one of the two mid-fidelity models will be developed and used. One

possible model will involve a larger set of CFD runs and will combine a BEM solver with lookup tables generated from the CFD solutions. The second possible model will not involve additional CFD runs and will use OLAF.

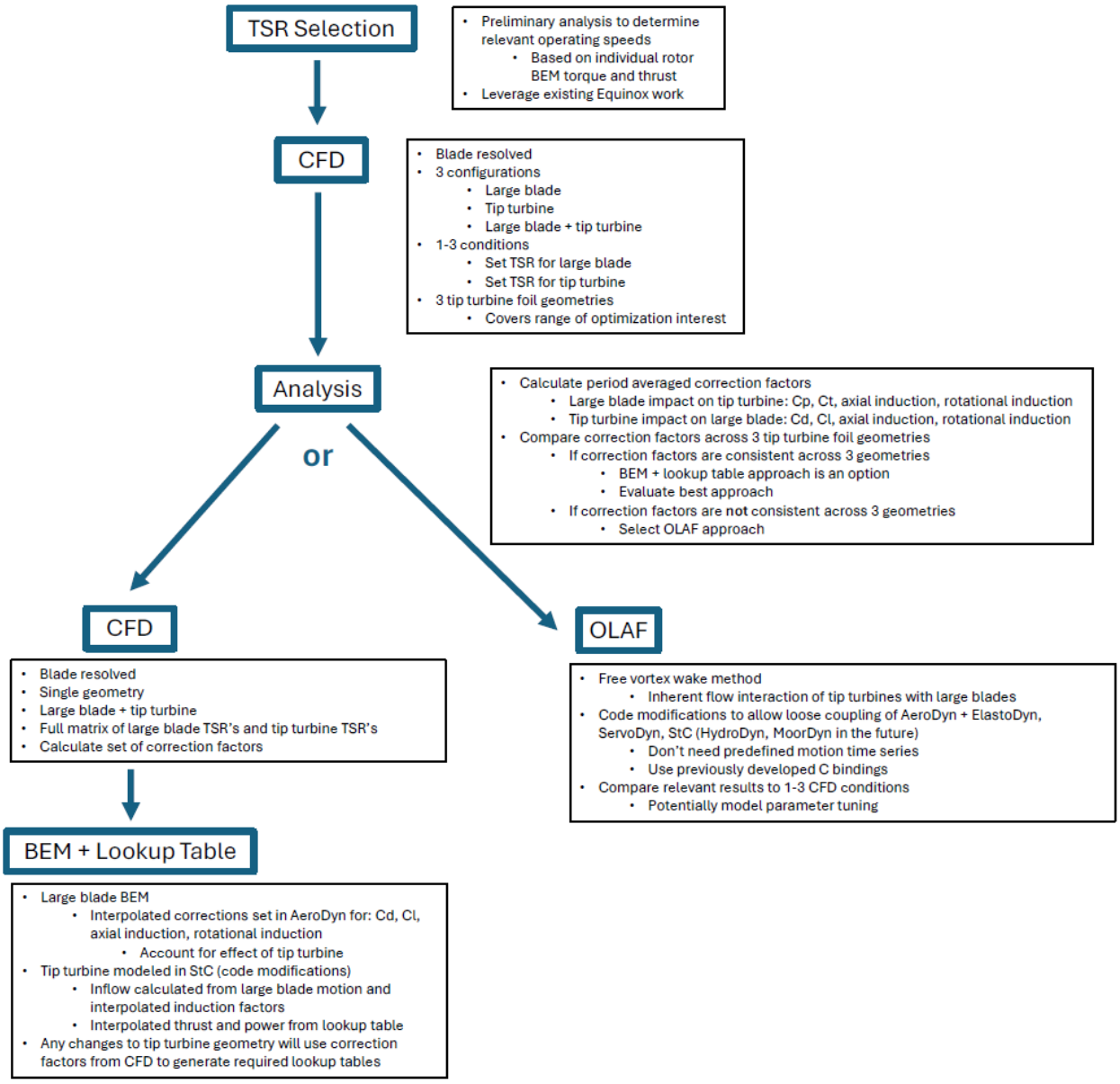

Figure 2. Numerical analysis workflow (TSR = tip-speed ratio, Cp = power coefficient, Ct = thrust coefficient, Cd = drag coefficient, Cl = lift coefficient)

The CFD will be performed with the commercial code STAR-CCM+ and will have a steady uniform inflow velocity. A three-dimensional unsteady Reynolds-averaged Navier-Stokes formulation will be used with a k-ω shear stress transport turbulence closure model. The mesh will feature boundary layer refinement on all blade surfaces including finer resolution at the leading and trailing edges of all foils and at the tip of

the large blade. The boundary layer mesh should result in a sufficiently small y+ value, but all y+ wall treatment will be active.

The CFD domain will be a half cylinder enclosing half of the system (one large blade and one tip turbine). One of the half circles will be a velocity inlet and the other will be a pressure outlet. The rectangular cut section will have a periodic boundary condition. The outer far-field surface will have a slip wall condition. The large-blade motion will be captured with rigid-body rotation of the full domain, and the tip turbine motion will be captured with a sliding interface and the superposition of the rigid-body motion.

The CFD will be run for three overall configurations: only one large blade, only one tip turbine, and half of the full system, including both one large blade and one tip turbine. The runs with the individual components establish baseline characteristics for the loads and the induction factors. The difference between the run with the combined components and the individual components can then establish the effects of the tip turbine on the large blade and the effects of the large blade on the tip turbine. For the large blade, correction factors will be calculated for lift, drag, axial induction and rotational induction. For the tip turbine, correction factors will be calculated for thrust, torque, axial induction, and rotational induction.

The ultimate goal is to have a model that can be used for foil optimization. One proposed option is a hybrid model with BEM for the large blade and CFD-informed applied loads for the tip turbine. This approach would be computationally inexpensive, allowing quick optimization with a set of load cases. However, the method requires CFD runs for a full tip-speed ratio (TSR) matrix, which is not feasible to rerun for different geometric iterations. To evaluate if this option could be accurate enough to consider, normalized correction factors need to be compared across a range of potential foil shapes. In the initial CFD, three tip turbine foil shapes will be tested, covering the extents of the expected parameter domain. If the normalized correction factors are significantly different, the OLAF-based option will be selected. If the normalized correction factors are similar, both options will be considered further.

If the BEM + lookup table approach is selected, a full TSR matrix will be run for a single geometry, and a full matrix of correction factors will be calculated. The standard AeroDyn BEM model will be used for the large blade, but corrections will be made to the lift, drag, and induction coefficients for the blade elements in the tip turbine region, based on values interpolated from the CFD-based correction factor matrix. The inflow to the tip turbines will be calculated from the CFD data using the large-blade motion, with the addition of the interpolated induction factors. The torque and thrust will then be calculated from the lookup tables and applied to the large blade through the StC module. Tip turbine data will be output for performance analysis. Some code modifications will be needed to allow these loads to be updated at each time step, as the StC module currently allows only a predefined time series.

If the OLAF approach is selected, no more CFD will be run. The existing CFD data can be used for FVW model parameter tuning and can be used as a verification for relevant TSR conditions. The existing code allows an arbitrary definition of lifting lines, but only a conventional single-stage rotor can be coupled to the ElastoDyn structural solver. Complex wing definitions, like the EQOT two-stage rotor, cannot be coupled to the structural motions and instead require a predefined position time series. This will be addressed using a new wrapper code that takes advantage of existing C bindings to allow the foil positions to be updated at each time step. Three instances of ElastoDyn, one for each rotor, will be called at each

time step. This method will only include rigid-body motion, but the setup will be useful for future expansions to flexible blades. The FVW technique will inherently model interactions between the shed vortices of the large-blade tip and the small tip turbine. It is expected that this method will capture the complex flow interactions, which can be verified with qualitative and quantitative comparisons to the existing CFD. For optimization, the OLAF approach is more computationally expensive, leading to slower design iterations. However, this model is more robust; the accuracy of this method should be relatively unaffected by changes in tip turbine foil shape.

6.2 Test and Analysis Matrix and Schedule

Figure 3 shows the matrix of load cases that will be run in the initial CFD step of the project. The results of these load cases will inform which mid-fidelity model is selected, and will serve as verification data. The complex flow field will be captured, and flow phenomena can be visualized. Some TSR selection will be required before running these load cases. The net torque at the main rotor shaft needs to be near zero, with the induced torque from tip turbine thrust equal and opposite to the hydrodynamic torque on the main rotor blade. The main rotor torque will be checked in the CFD simulations to ensure that this condition is met. Initial estimates of the rotation speeds for the two rotors will be based on calculations using torque and thrust values from single-stage rotors with a simple inflow. Prior work done by EQOT will be used to inform this process.

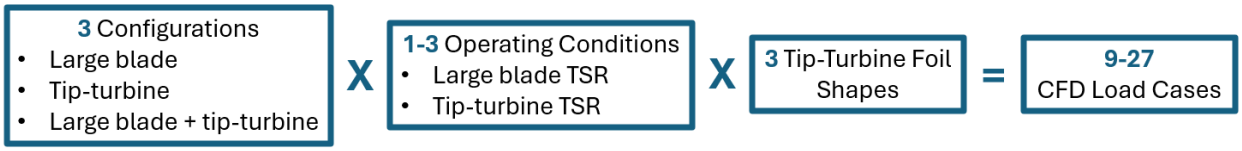

Figure 3. Initial CFD test matrix

If the BEM + Lookup Table method is selected, the CFD load cases described in Figure 4 will be run to determine the lookup table correction factors. The mid-fidelity load cases described in Figure 5 will then be run.

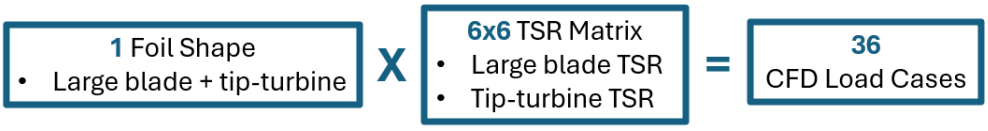

Figure 4. CFD test matrix to support BEM + lookup table method

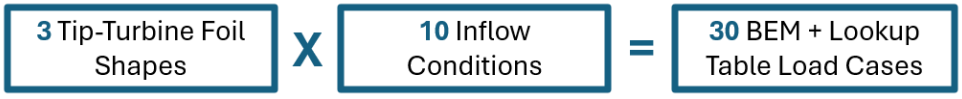

Figure 5. BEM + lookup table mid-fidelity model test matrix

If the FVW method is selected, then the mid-fidelity load cases described in Figure 6 will be run.

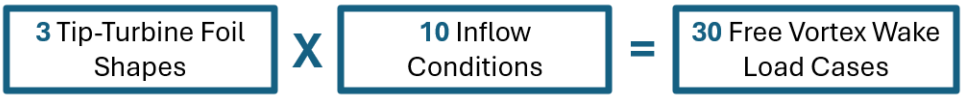

Figure 6. FVW mid-fidelity model test matrix

The planned schedule for each phase of work is given in the Gantt chart in Table 1. All modeling and post-processing work will be performed by NLR. EQOT and NLR will meet together to discuss the progress of the work and determine if the appropriate level of detail is being captured. The planned start date is shown in the chart but may need to be shifted in the event of delays in foreign partner contract approvals. If the start date is shifted, the rest of the work will also be appropriately shifted.

	August				September				October				November				December				January				February				March				April			
Tasks	WK 1	WK 2	WK 3	WK 4	WK 5	WK 6	WK 7	WK 8	WK 9	WK 10	WK 11	WK 12	WK 13	WK 14	WK 15	WK 16	WK 17	WK 18	WK 19	WK 20	WK 21	WK 22	WK 23	WK 24	WK 25	WK 26	WK 27	WK 28	WK 29	WK 30	WK 31	WK 32	WK 33	WK 34	WK 35	WK 36
Data and Geometry Transfer																																				
Preliminary BEM for TSR Selection																																				
CFD: Case Setup																																				
CFD: Convergence Study																																				
CFD: Run																																				
Post-Processing / Correction Factor Analysis																																				
Reduced-Order Model Selection																																				
Reduced-Oder Model: Code Modifcations																																				
Reduced-Order Model: Setup																																				
Reduced-Order Model: Running																																				
Post-Processing / Verification																																				
Writing and Reporting																																				
Post Access Report																																				
Post Access Questionnaire																																				

Table 1. Project Gantt chart

6.3 SAFETY

All work will be numerical and no relevant safety procedures are required.

6.4 CONTINGENCY PLANS

The main rotor of the EQOT turbine should have a net near-zero torque in steady-state operations. The induced torque from the tip turbine thrust should be equal to and opposite of the main rotor hydrodynamic torque. In a physical system, at given inflow speed and a given tip turbine rotation speed, the main rotor rotation speed will converge to a value that balances the main rotor torque and the tip rotor thrust. This condition will be checked in the initial CFD phase with the selected fixed rotation speeds for the two stages. If the selected speeds result in an unacceptably large net torque in the CFD, then a rigid-body motion solver can be used for the main rotor. This will result in longer required simulation times, increasing computation cost, but may be necessary to simulate a realistic steady-state operation condition. The zero-torque condition will naturally occur in the mid-fidelity model after some transient.

The initial CFD field will be used to identify the dominant flow interaction effects between the two stages of the system. The two mid-fidelity branches in the flow chart in Figure 2 are expected to be the best options leveraging existing code modules. It is possible that the initial CFD highlights some unexpected critical flow phenomena that cannot be captured with these proposed methods. In this case, there is some flexibility for the mid-fidelity model to be further adjusted by the CFD results.

6.5 Data Management, Processing, and Analysis

6.5.1 Data Management

Raw data will be stored on the NLR HPC where the simulations were performed. The raw data, particularly from the CFD, will be too large to be practically shared. The post-processing will also take place on the NLR HPC. Simulations will be run sufficiently long to reach rotation-averaged steady conditions with no effect of the transient. Correction factors and verification comparisons between the selected mid-fidelity model and the CFD will be based on time-averaged values over the last fixed number of large rotor rotations.

Table 2 lists the correction factors to be calculated from the CFD results. These corrections are the same for the initial CFD step and the CFD component of the BEM + lookup table method. If some additional metric stands out from observation of the CFD flow field, another quantitative parameter can be added to capture it. The first column lists tip turbine metrics. These metrics will be compared when the tip turbine is by itself and when the large blade is present to quantify the changes due to the large-blade flow patterns. The second column lists large-blade metrics. These metrics will be compared when the large blade is by itself and when the tip turbine is present to quantify the changes due to the tip turbine flow patterns.

Large-blade impact on tip turbine	**Tip turbine impact on large blade (near-tip sections)**
Cp	Cd
Ct	Cl
Axial induction	Axial induction
Rotational induction	Rotational induction

Table 2. Correction factors from CFD results (Cp = power coefficient, Ct = thrust coefficient, Cd = drag coefficient, Cl = lift coefficient)

The metrics listed in Table 3 will be saved for every load case that includes both the main rotor and the tip turbine rotor. These metrics will be used for verification of the selected mid-fidelity model through comparisons with the relevant CFD results.

	CFD	Mid-Fidelity
Tip Turbine Cp	3–9 Load Cases	30 Load Cases
Tip Turbine Ct	3–9 Load Cases	30 Load Cases
Tip Turbine RPM	3–9 Load Cases	30 Load Cases
Main Rotor RPM	3–9 Load Cases	30 Load Cases
Full System Cp	3–9 Load Cases	30 Load Cases
Full System Ct	3–9 Load Cases	30 Load Cases

Table 3. Time-averaged performance metrics (Cp = power coefficient, Ct = thrust coefficient, RPM = rotations per minute)

6.5.2 Data Processing

Convergence studies will be performed for the spatial and temporal discretization of the CFD simulations. These steps will create confidence in the high-fidelity results. The mid-fidelity results will be verified against the high-fidelity results to give EQOT confidence in the model for future design iterations.

All metrics described in Section 6.5.1 will be time-averaged over the last fixed number of large-rotor rotations. The metrics will be tracked through time to ensure that converged values are obtained. Load cases will only include time-steady inflows.

6.5.3 Data Analysis

All simulations will be performed at full scale, so no scaling is required.

Verification results will be the focus of a journal or conference publication. Normalized comparisons will be made between the metrics listed in Table 3 for the mid-fidelity model and the select CFD cases. This will include time-averaged values and time series. The correction factors derived from the CFD listed in Table 2 that are identified to be the most critical will also be discussed in the publication.

The mid-fidelity model will require a custom driver code to connect existing OpenFAST modules effectively for the two-stage turbine. This new driver code will be made publicly available without any specific EQOT input files to protect their intellectual property.

7 PROJECT OUTCOMES

7.1 RESULTS

7.1.1 Initial BEM

Geometry files for the baseline main rotor (MR) and secondary rotor (SR) blades were used to build blade definition files based on span, chord length, twist, out-of-plane offset, and in-plane offset. The blade was divided into 20 sections. Blade section profile coordinates were used to generate polars over a range of seven Reynolds numbers ranging from 5.0e4 to 5.0e7. Lift, drag, and moment coefficients were calculated

over a range of -30 to 30 degrees using XFOIL (MIT, 2025). The range of angles of attack was extended to -180 to 180 degrees using the AirfoilPrep Python tool (NLR, GitHub AirfoilPreppy, 2025).

Single-stage BEM simulations were run for the main rotor and secondary rotor over a range of 10 inflow speeds for the main rotor and 11 inflow speeds for the secondary rotor. These were run using the AeroDyn driver to sweep over 58 TSRs for the main rotor and 22 TSRs for the secondary rotor at each inflow speed.

Results of the initial BEM simulations, including power, thrust, blade loading, and induction, are compared to CFD results in the following sections.

7.1.2 CFD

The CFD setup followed the plan outlined in Section 6.1. For the single-stage CFD, only a single blade was modeled utilizing periodic boundary conditions on the flat boundaries shown in Figure 7 and a rotating reference frame. The domains were 20 rotor diameters (D) in length and had a radius of 5D. This radius results in a blockage of 0.01, which should have negligible effects. The single-stage main rotor mesh had 4.68 million cells, and the single-stage secondary rotor mesh had 3.16 million cells.

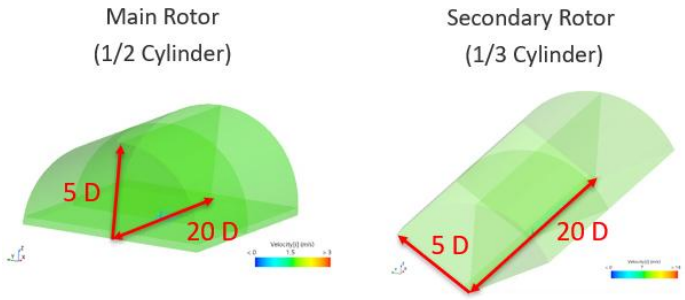

Figure 7. CFD domain shape and dimensions

Each blade was divided into 20 sections (including one hub section) matching the discretization used in the BEM model. Forces and moments were recorded in three directions for each segment. Induction was measured by sampling the flow velocity before and after the rotor. The velocity was sampled for 20 annuli at six locations upstream of the rotor and six locations downstream of the rotor, as shown in Figure 8. The surface averaged axial and tangential velocities were recorded for all annuli.

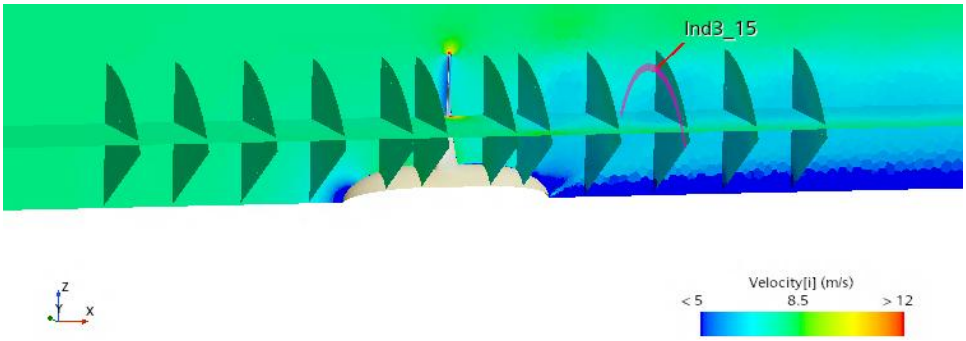

Figure 8. Induction sampling annuli

7.1.2.1 Single Stage

In order to understand the interaction effects of the combined-stage system, the loads of each rotor need to be characterized in a single-stage configuration. Figure 9 shows the power and thrust coefficient comparison between CFD and BEM over a range of TSRs for the main rotor. BEM results are included with a range of inflow velocities, while CFD results are only for a single velocity. There is generally good agreement in the power curve, with BEM slightly underpredicting maximum power and at a slightly lower peak TSR. BEM tends to underpredict thrust at high TSRs.

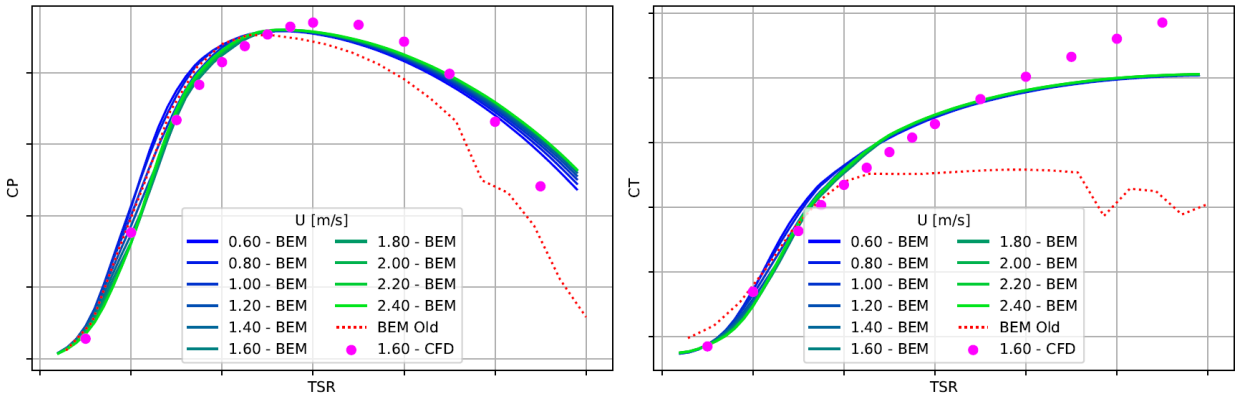

Figure 9. Single-stage CFD: Main rotor Cp and Ct curves compared to BEM predictions made in OpenFAST (OF) and previous EQOT predictions made with Blade Optimization Tool

Figure 10 shows the same comparisons for the single-stage secondary rotor. The BEM results see a spike in loads for both the power and thrust at a TSR below the peak. This spike shows up in the BEM results for all but the lowest inflow velocity. This effect is thought to be related to the transition to turbulent Reynolds numbers combined with the specific twist profile. In the CFD, which was run at a higher velocity where the spike occurs in the BEM results, it is thought that 3D effects not captured in the BEM smooth out the transition in loads, and there is no spike. Besides this effect, there is also a reasonable match in the power, thrust, and peak TSRs.

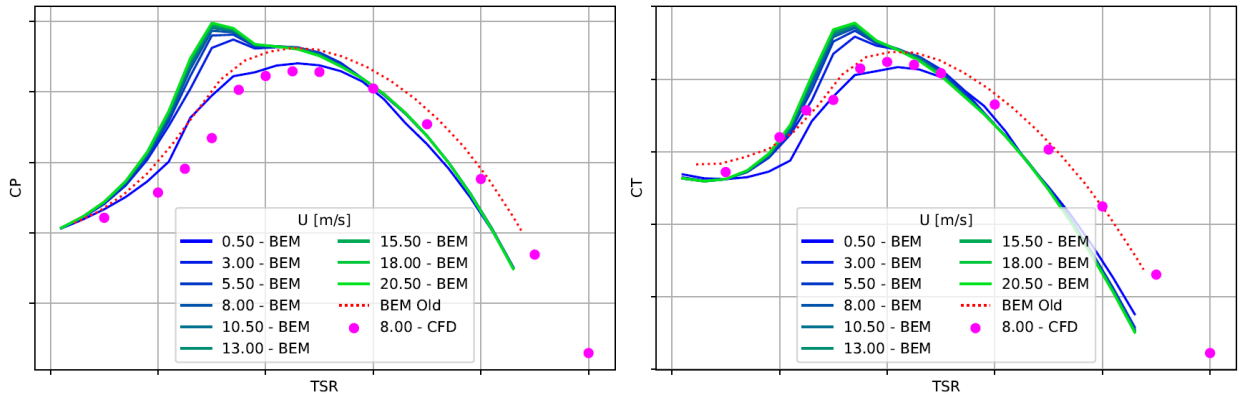

Figure 10. Single-stage CFD: Secondary rotor Cp and Ct curves compared to BEM predictions made in OpenFAST (OF) and previous EQOT predictions made with Blade Optimization Tool

Induction cannot be sampled exactly from a CFD simulation at the exact location of the rotor. Axial induction was originally calculated following the technique described in a 2021 paper by Medes et al., where the velocity at the location of the blade is extrapolated from an exponential fit of all velocities upstream of the rotor (Mendes, Macias, Oliveira, & Brasil, 2021). It was found that simply interpolating the velocity from the upstream and downstream samples provided a more reasonable result. Plots of axial induction across the sampling points are shown for the main rotor in Figure 11 and for the secondary rotor in Figure 13. Tangential induction was found to be near zero at all upstream sampling points. The tangential velocity at the location of the rotor was simply taken as the value at the closest sampling point downstream of the rotor. Plots of tangential induction are shown for the main rotor in Figure 12 and for the secondary rotor in Figure 14.

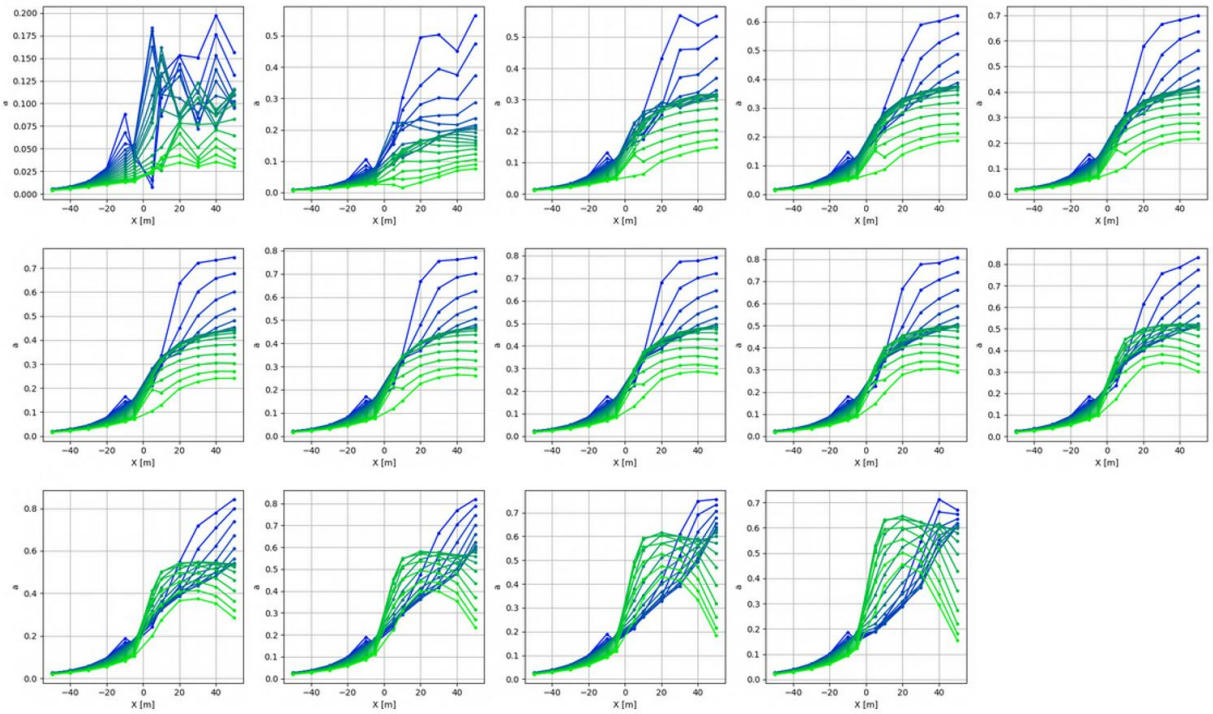

Figure 11. Single-stage CFD: Main rotor axial induction factor (color progression from blue at the root to green at the tip, increasing TSR from upper left to lower right subplot)

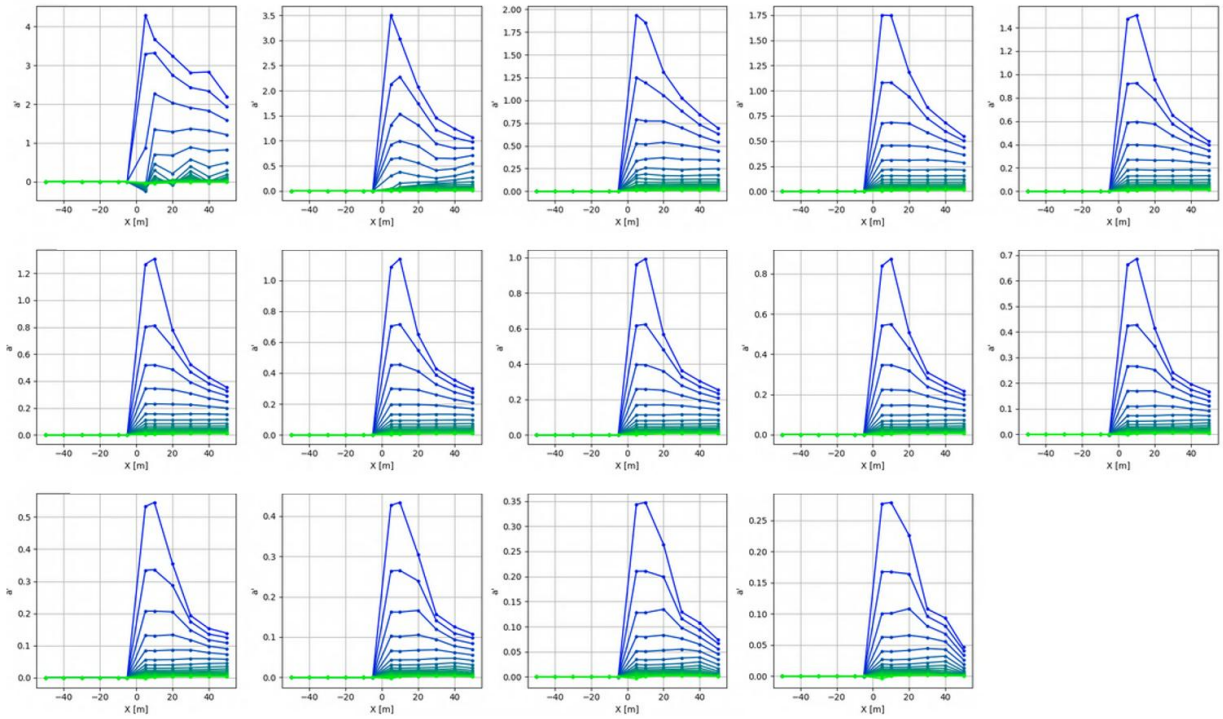

Figure 12. Single-stage CFD: Main rotor tangential induction factor (color progression from blue at the root to green at the tip, increasing TSR from upper left to lower right subplot)

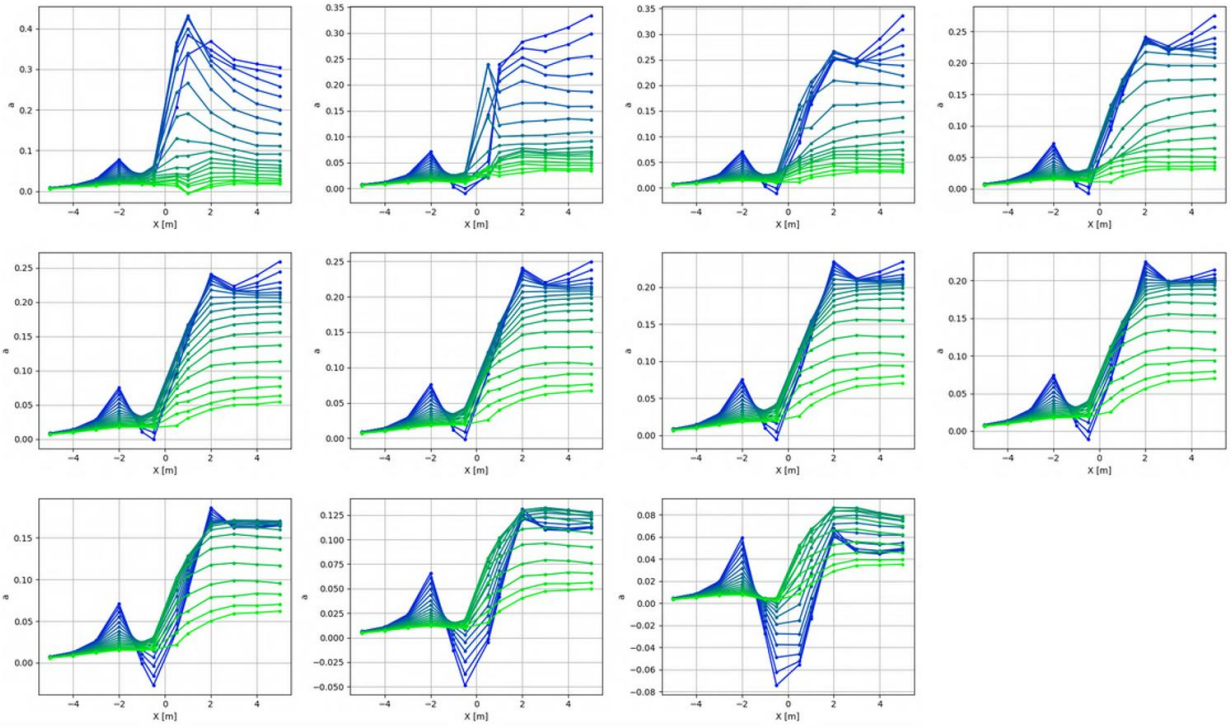

Figure 13. Single-stage CFD: Secondary rotor axial induction factor (color progression from blue at the root to green at the tip, increasing TSR from upper left to lower right subplot)

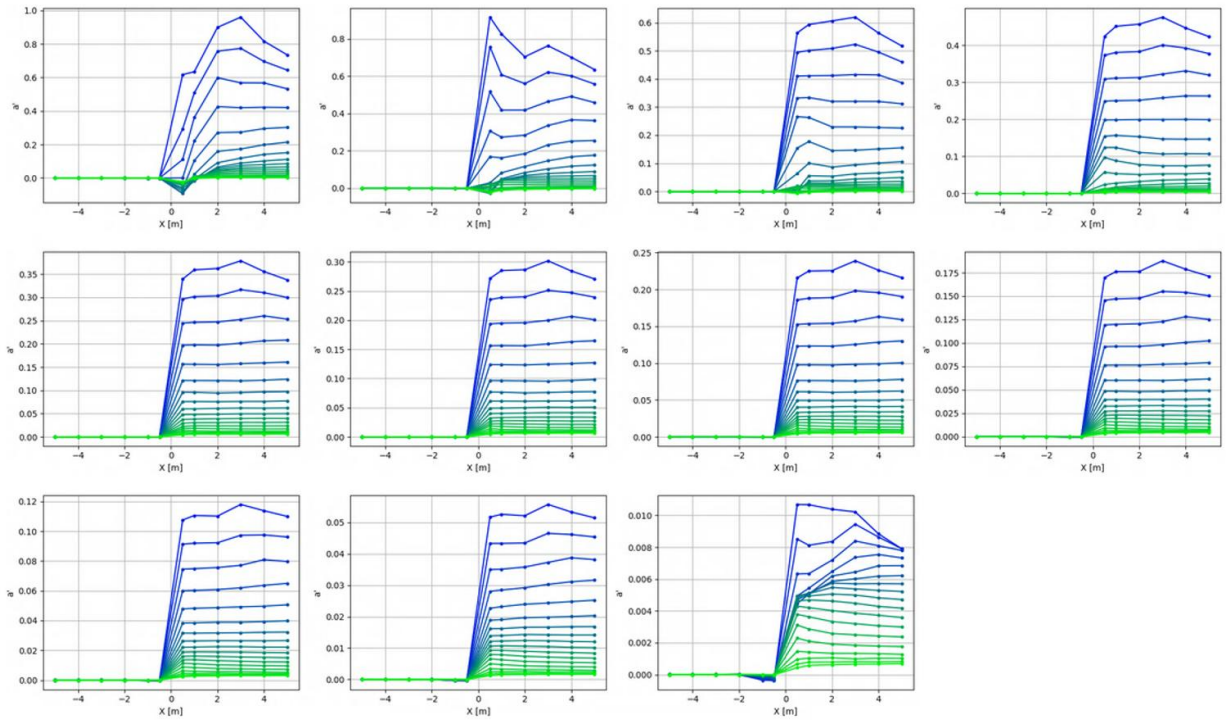

Figure 14. Single-stage CFD: Secondary rotor tangential induction factor (color progression from blue at the root to green at the tip, increasing TSR from upper left to lower right subplot)

From the single-stage main rotor CFD, it is also useful to check the induced velocity at the location of the secondary rotor plane in the secondary rotor reference system. This predicts what kind of changes to the relative inflow the secondary rotor may experience from the presence of the main rotor. Figure 15 shows this across a range of main rotor TSRs for the secondary rotor axial and tangential directions. The axial-induced velocity, shown in blue, shows the deficit from the wake of the main rotor trailing edge, which for relevant main rotor TSRs is negative near the secondary rotor hub but positive near the secondary rotor tip. The tangential-induced velocity, shown in orange, shows the flow rotation from the main rotor tip vortex. Note that the changes to the velocity are not uniform across the secondary rotor span. For relevant main rotor TSRs the shape and core radius of the tip vortex are visible, which is useful for the setup of a mid-fidelity FVW model. The shape matches that of a viscous tip vortex, with a core radius of about 0.3 of the secondary rotor span. This spanwise distribution inspired the altered twist profile geometry variation mentioned in Section 7.1.2.2.

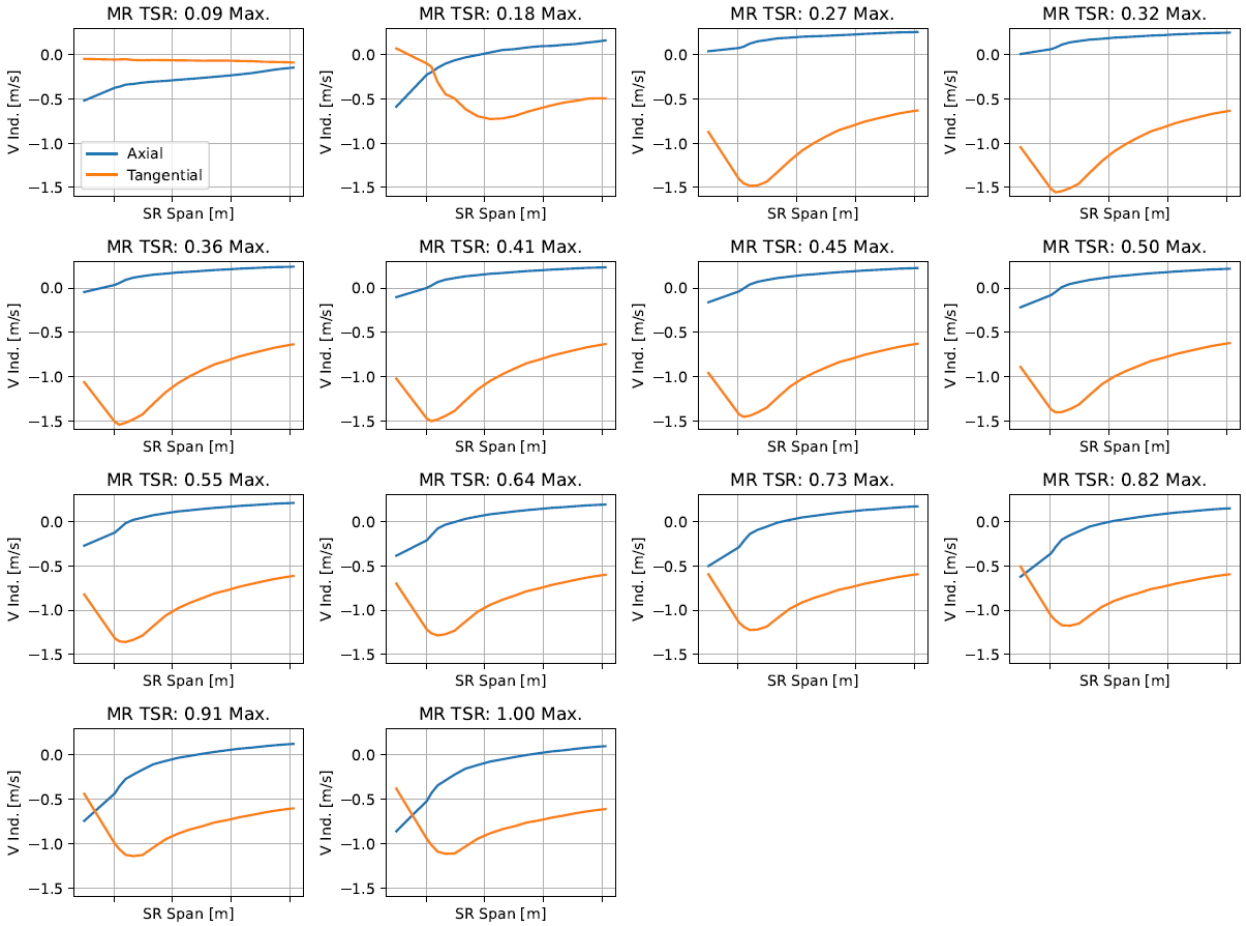

Figure 15. Single-stage CFD: Induced velocity in the axial and transverse directions along the secondary rotor span, as measured in the main rotor single-stage CFD at the location of and in the reference from of the secondary rotor, across a range of main rotor TSRs

Comparisons of the forces and induction along the main rotor and secondary rotor span, as predicted by BEM and CFD, are included in Section 7.1.2.2 along with the results from the combined-stage CFD.

7.1.2.2 Combined Stage

Combined-stage CFD used the same half-cylinder domain as used for the single-stage main rotor simulation and shown in Figure 7. For the main rotor motion, a rotating reference frame was used again with the periodic boundary conditions, and only a single blade was modeled. For the secondary rotor, in order to predict realistic interactions, the full three-bladed rotor was modeled using a sliding cylindrical interface to the outer main rotor domain with prescribed motions. With more resolved blades, and more requirements for wake refinement, the combined-stage CFD mesh had a considerably larger 20.59 million cells. In addition to a larger mesh, a timescale mismatch significantly increased computation cost. The simulation needs to be run long enough for the main rotor wake to develop, but with a short enough time step to resolve the flow changes around the secondary rotor. Figure 16 shows a visualization of a vorticity threshold from the combined-stage CFD, where the tip vortices from the two stages are clearly visible. Some interruption or alteration of the shed vorticity from the trailing edge of the main rotor is also visible near the secondary rotor.

Figure 16. Vorticity threshold visualization from combined-stage CFD highlighting tip vortices shed from both the main rotor and secondary rotor

For all combined-stage simulations, the main rotor speed was held fixed, and the secondary rotor speed was iterated until the system came to equilibrium, where the period-averaged secondary rotor thrust (creates torque on the main rotor axis) exactly canceled the main rotor torque. Initial rotation speed predictions were made from the single-stage CFD loads. A coarse time step matching the scale of the main rotor was used for an initial time, to more efficiently develop the main rotor wake, with inaccurate resolution of the secondary rotor loads and wake. After this initial large-scale wake development, the time step was lowered to resolve the secondary rotor flow. At this time the secondary rotor speed was iterated to converge to a system torque equilibrium. The rotation speed was updated after five secondary rotor revolutions and adjusted with a correction based on the averaged loads over the last secondary rotor period.

Figure 17 shows the final secondary rotor TSR with a balanced torque on the main rotor shaft, along with the system power and thrust coefficients. The prediction based on the BEM loads is shown as well as three predictions made using the single-stage CFD loads. Two of the predictions with single-stage CFD loads include an adjustment for the relative rotational flow about the secondary rotor axis as measured in the main rotor single-stage CFD. One of these iterations is a prediction of the equilibrium point when the secondary rotor rotates with the tip vortex, and one is when it rotates in the opposite direction. The plot includes full combined-stage CFD for nine load cases. These include three main rotor TSRs each for the original geometry with a positive secondary rotor rotation direction, the original geometry with a negative rotation direction, and an altered secondary rotor twist profile with a positive secondary rotor rotation direction.

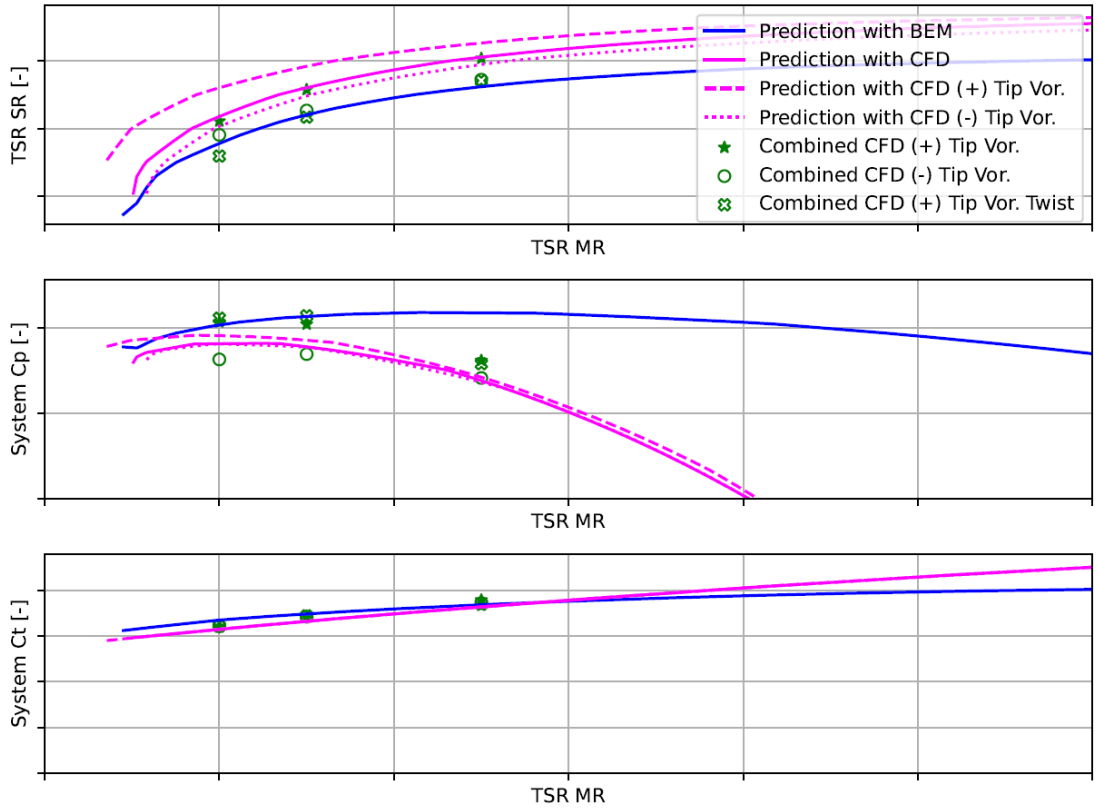

Figure 17. Combined-stage CFD: system equilibrium speeds, power coefficient, and thrust coefficient as predicted with single-stage BEM loads, single-stage CFD loads, and full combined-stage CFD. Results include three configurations of rotation direction and secondary rotor geometry.

Figure 18–Figure 35 show the spanwise distribution of tangential and normal forces and the axial- and tangential-induced velocities for all combined-stage CFD simulations. The resulting values from the combined-stage CFD are compared to those from the single-stage CFD and the single-stage BEM. Each of the three configurations ("Original" = original geometry with a positive secondary rotor rotation direction, "Reverse" = original geometry with a negative rotation direction, and "Twist" = altered secondary rotor twist profile with a positive secondary rotor rotation direction) were run for three main rotor TSRs. In these plots, the unsteady combined-stage CFD results include error bars that show the minimum and maximum values of the relevant value. This variability comes from the passage of the secondary rotor blade through the main rotor tip wake and is not present in the single-stage simulations.

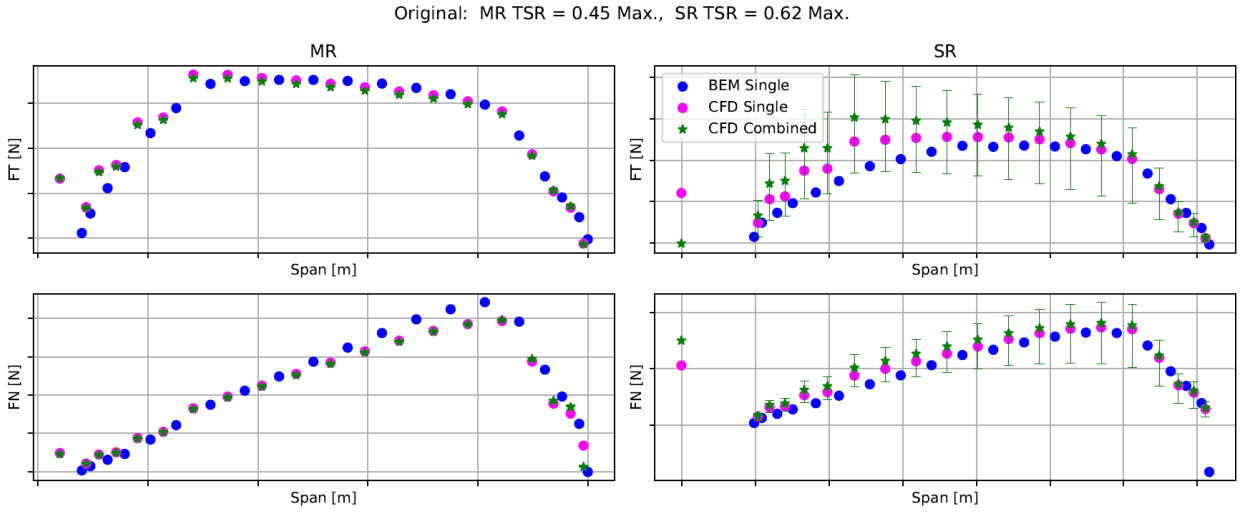

Figure 18. Combined-stage CFD – original TSR A: spanwise blade load distribution

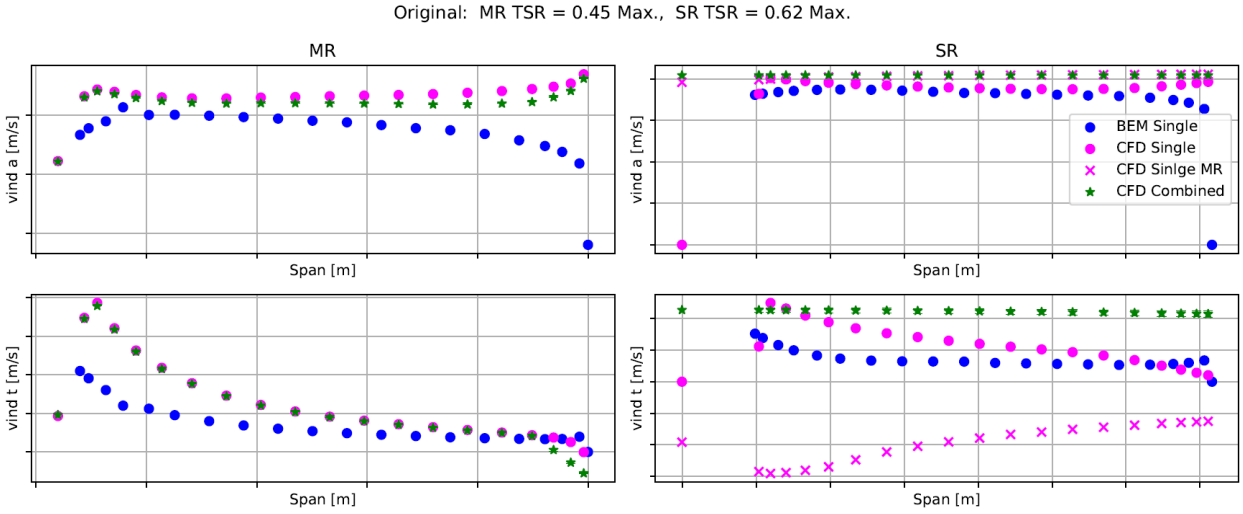

Figure 19. Combined-stage CFD – original TSR A: spanwise-induced velocity distribution

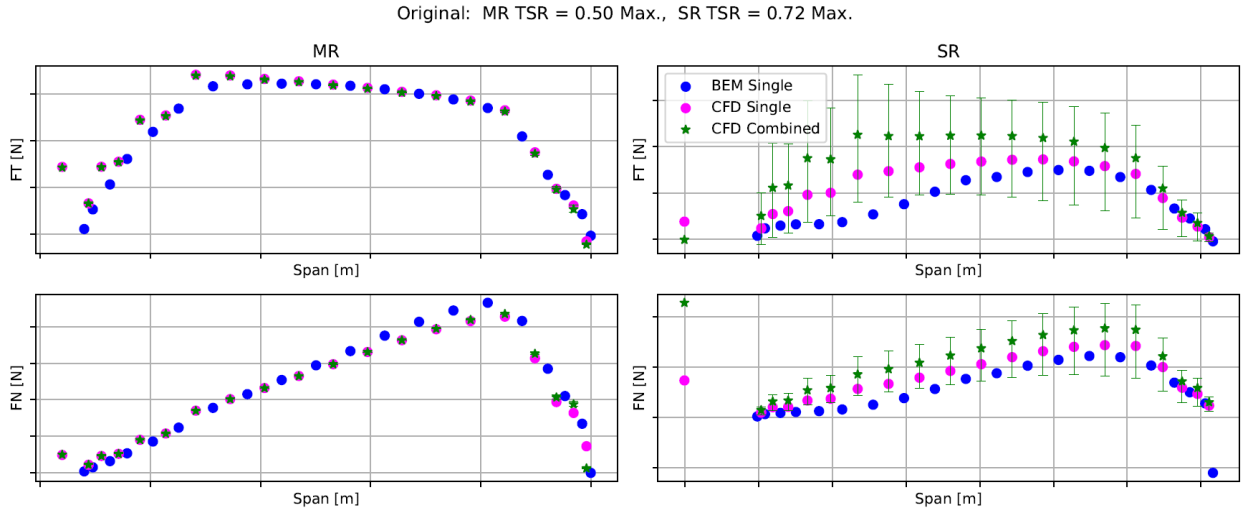

Figure 20. Combined-stage CFD – original TSR B: spanwise blade load distribution

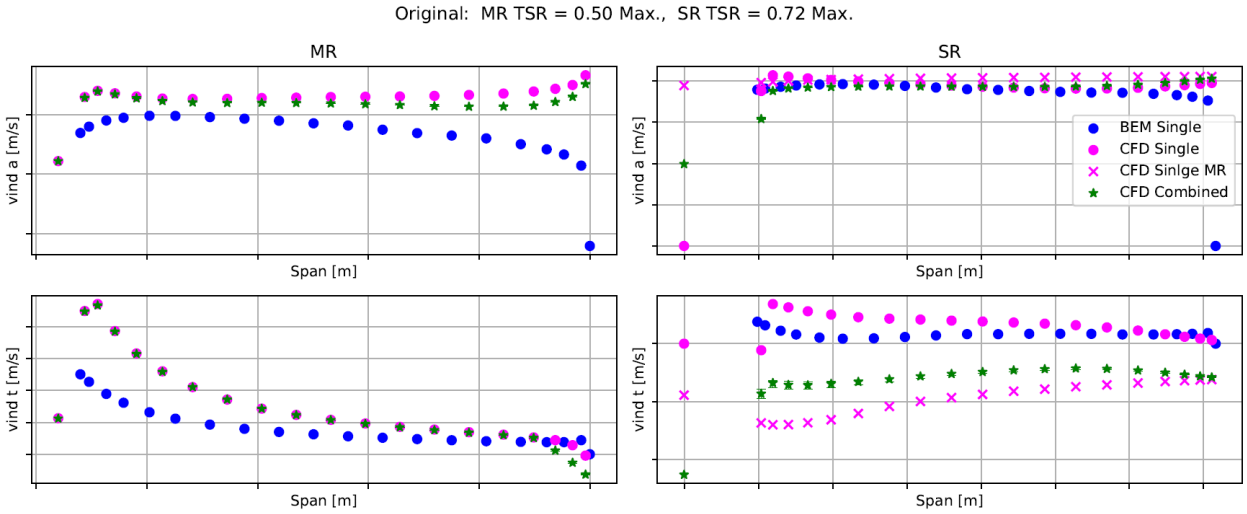

Figure 21. Combined-stage CFD – original TSR B: spanwise-induced velocity distribution

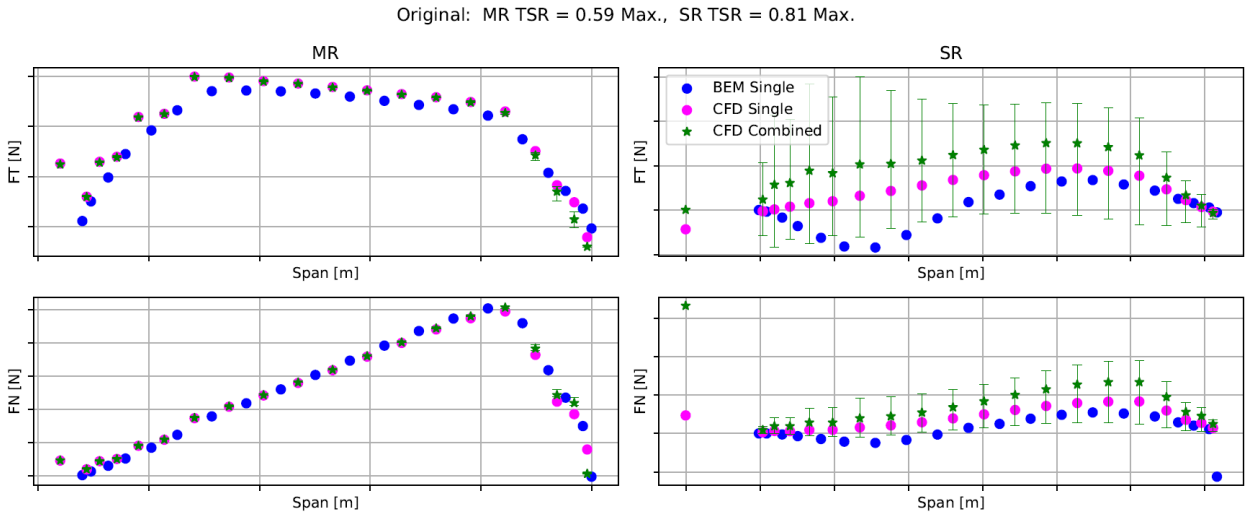

Figure 22. Combined-stage CFD – original TSR C: spanwise blade load distribution

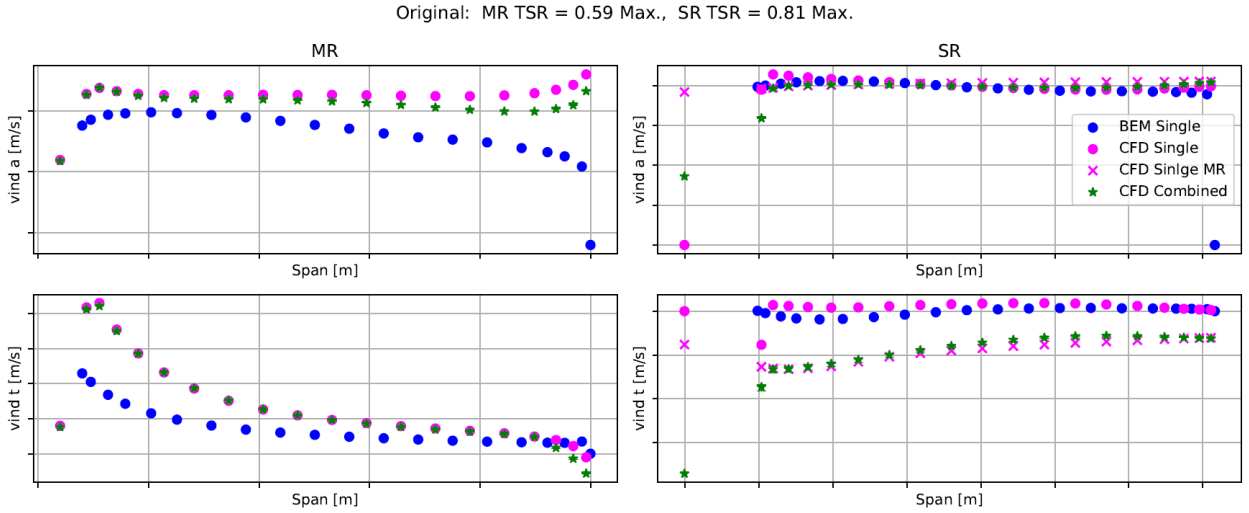

Figure 23. Combined-stage CFD – original TSR C: spanwise-induced velocity distribution

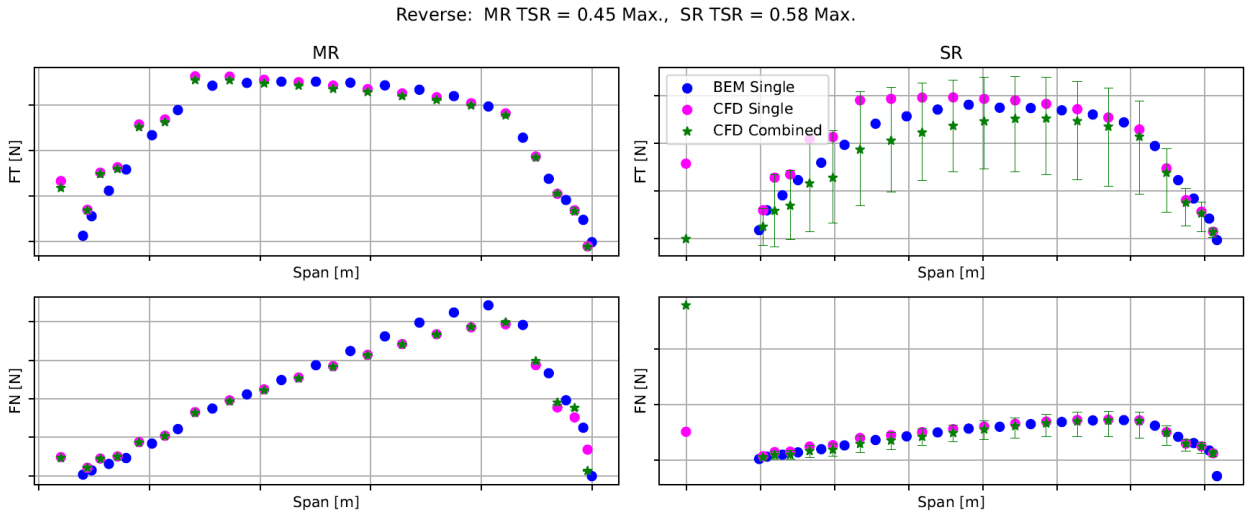

Figure 24. Combined-stage CFD – reverse TSR A: spanwise blade load distribution

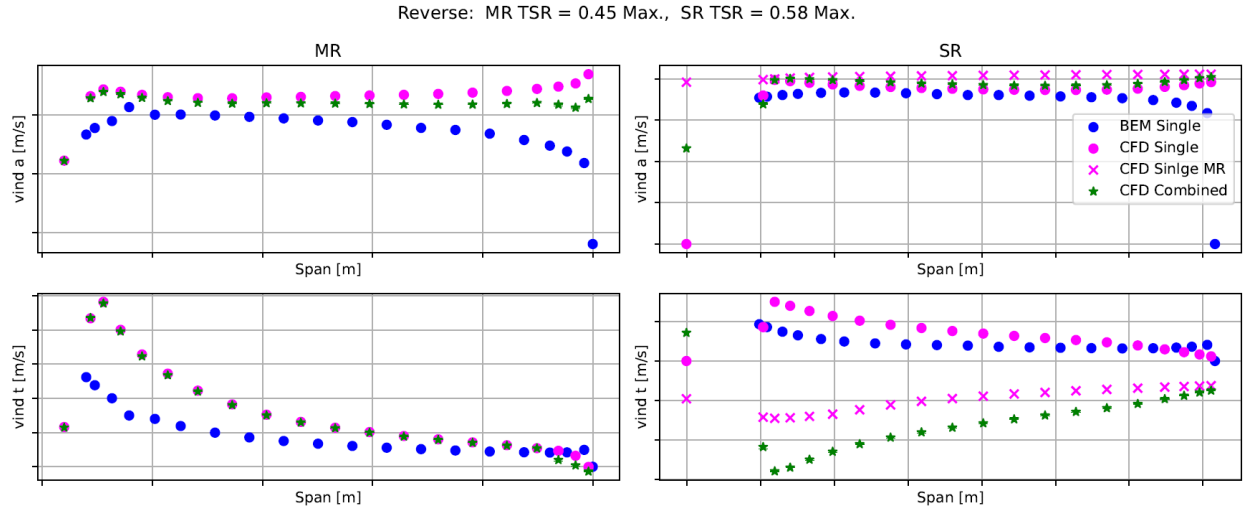

Figure 25. Combined-stage CFD – reverse TSR A: spanwise-induced velocity distribution

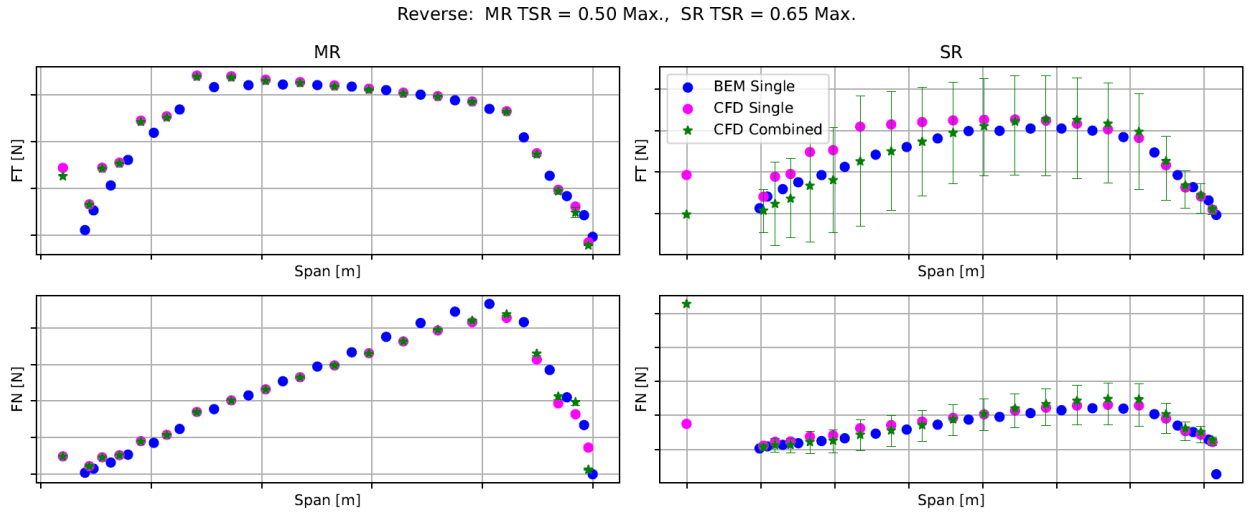

Figure 26. Combined-stage CFD – reverse TSR B: spanwise blade load distribution

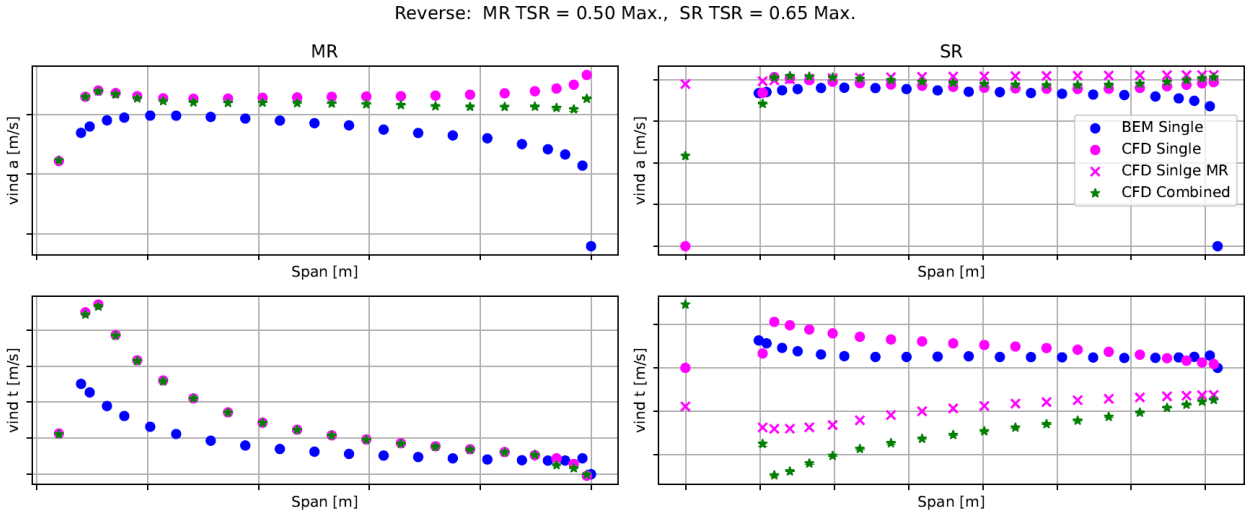

Figure 27. Combined-stage CFD – reverse TSR B: spanwise-induced velocity distribution

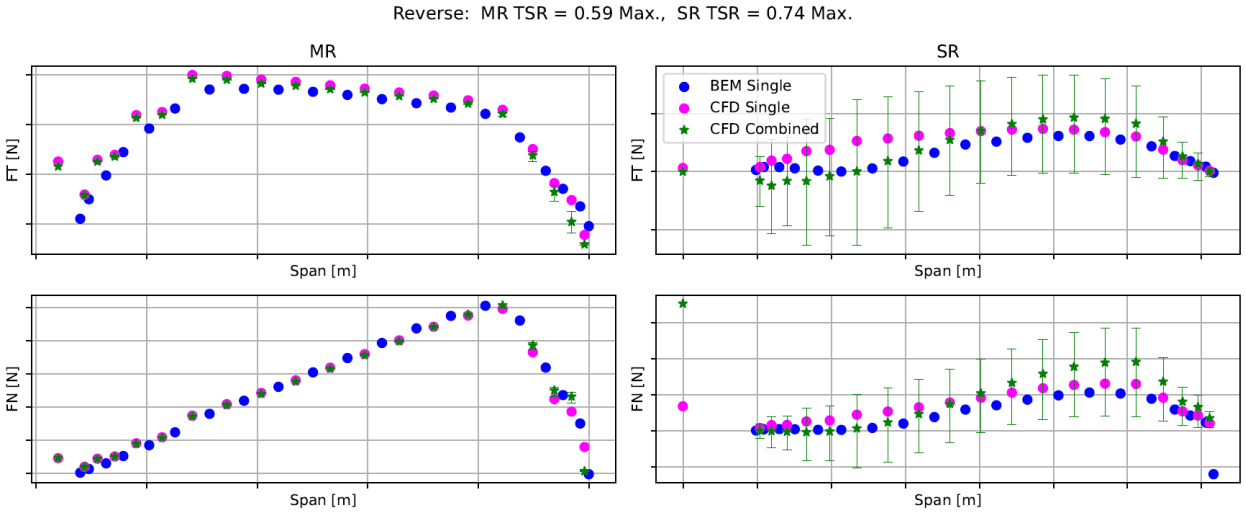

Figure 28. Combined-stage CFD – reverse TSR C: spanwise blade load distribution

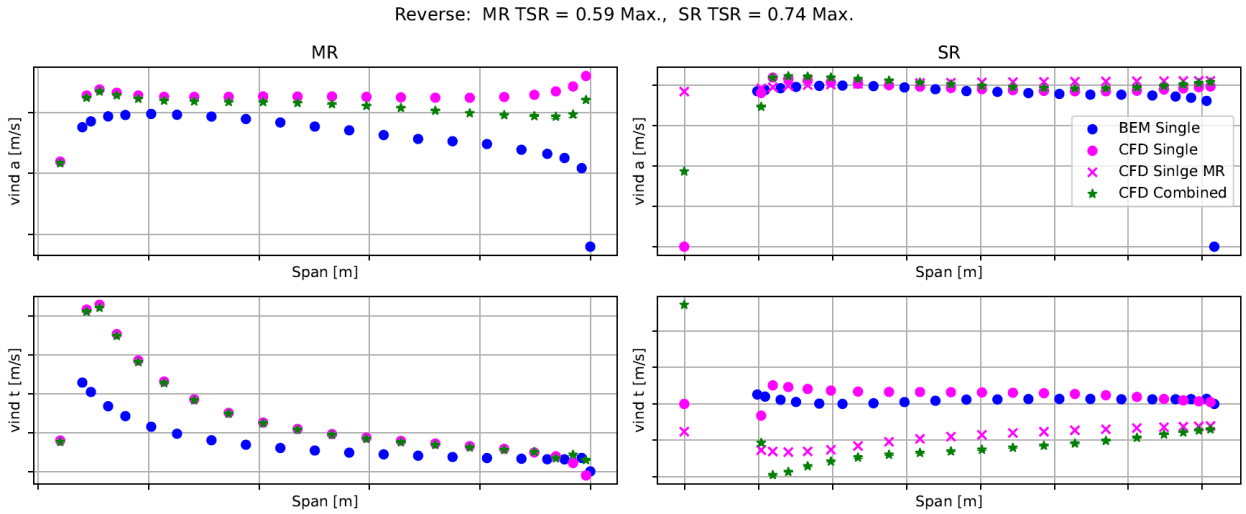

Figure 29. Combined-stage CFD – reverse TSR C: spanwise-induced velocity distribution

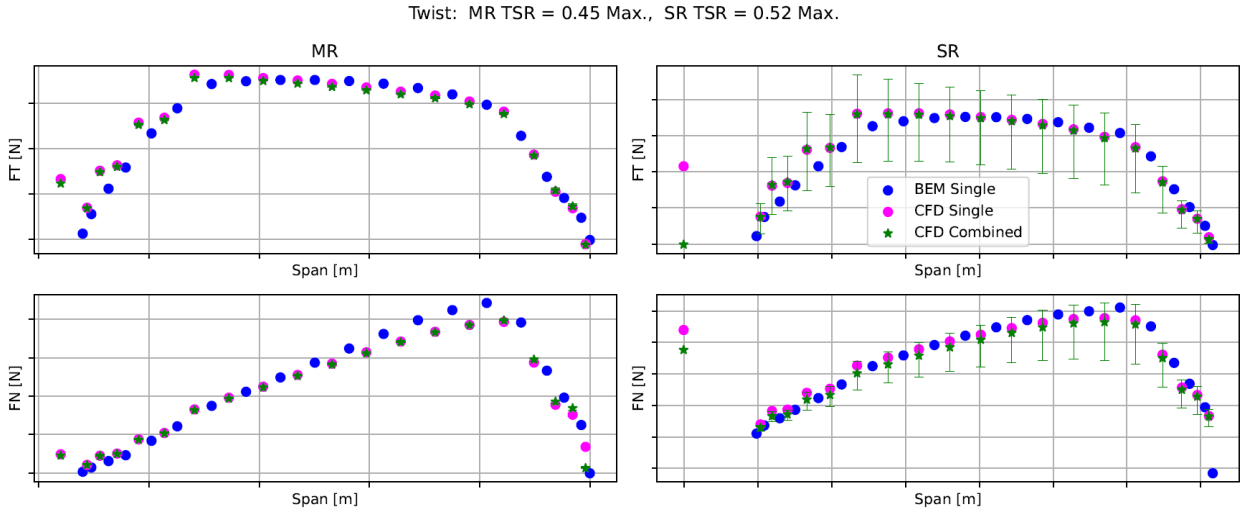

Figure 30. Combined-stage CFD – twist TSR A: spanwise blade load distribution

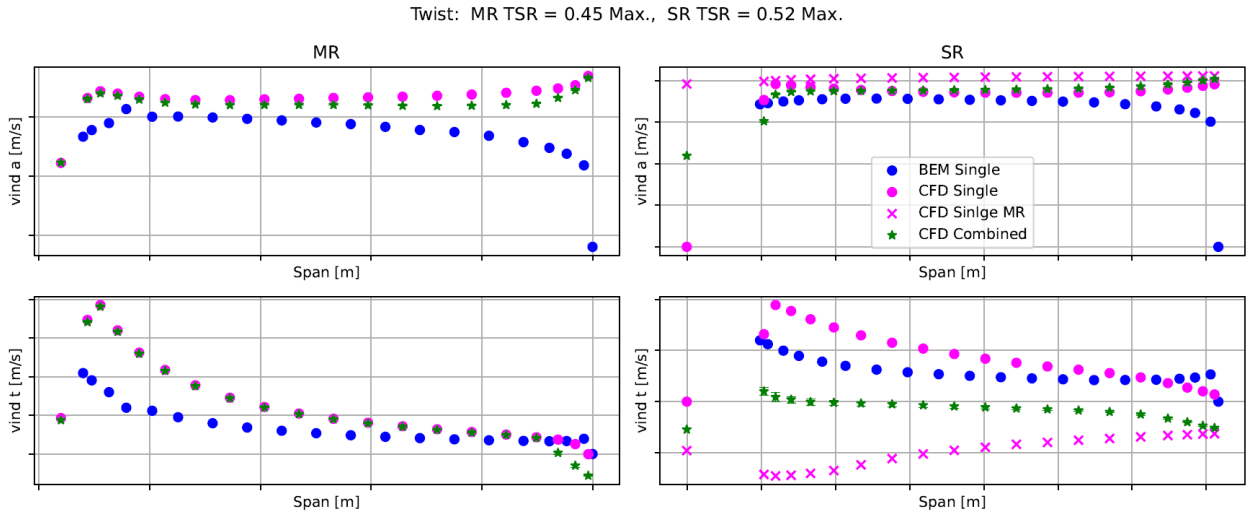

Figure 31. Combined-stage CFD – twist TSR A: spanwise-induced velocity distribution

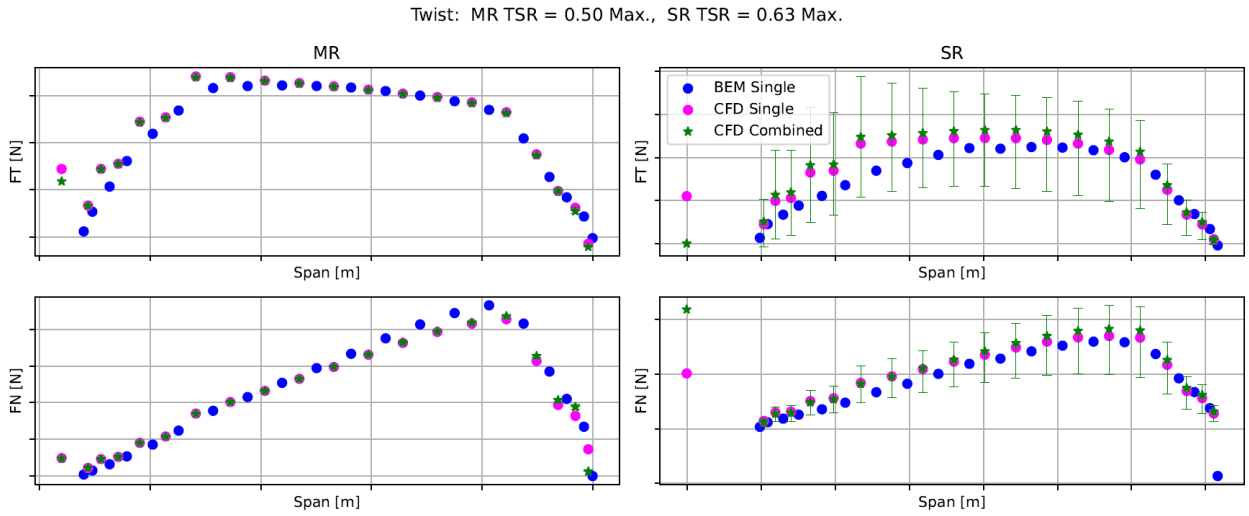

Figure 32. Combined-stage CFD – twist TSR B: spanwise blade load distribution

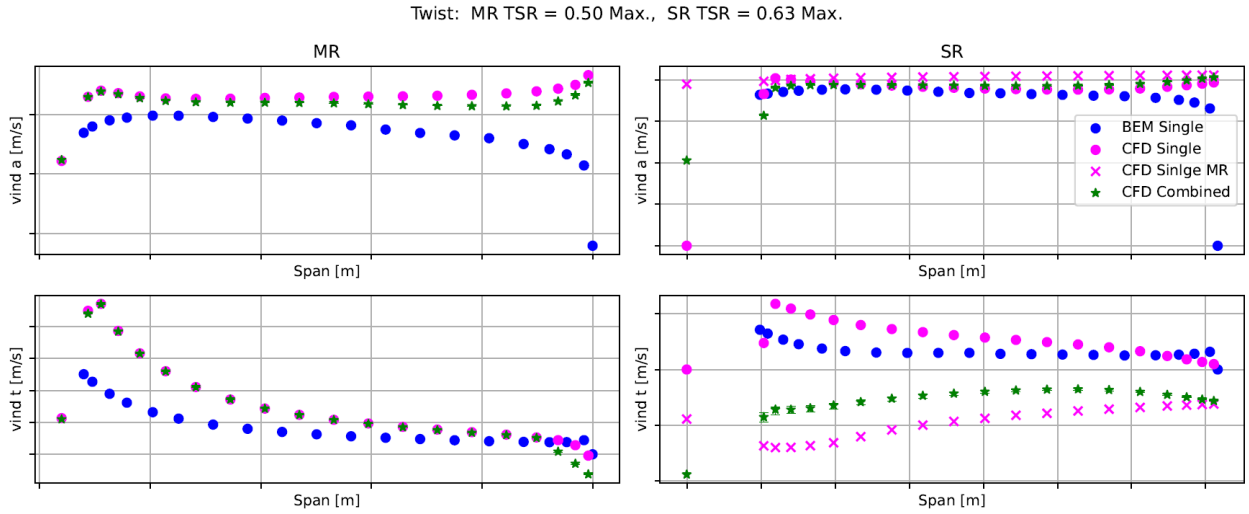

Figure 33. Combined-stage CFD – twist TSR B: spanwise-induced velocity distribution

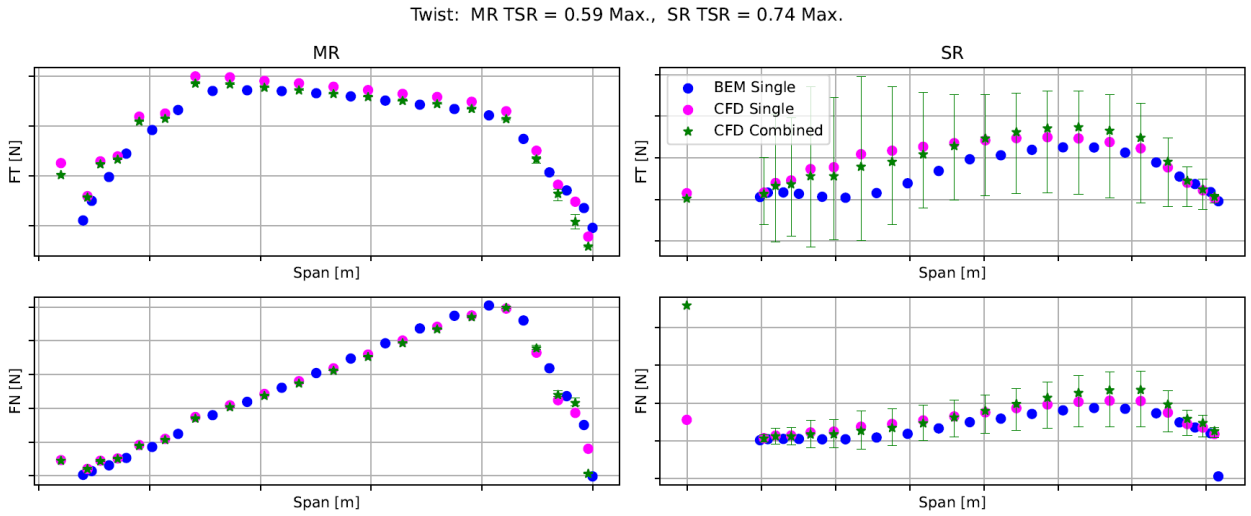

Figure 34. Combined-stage CFD – twist TSR C: spanwise blade load distribution

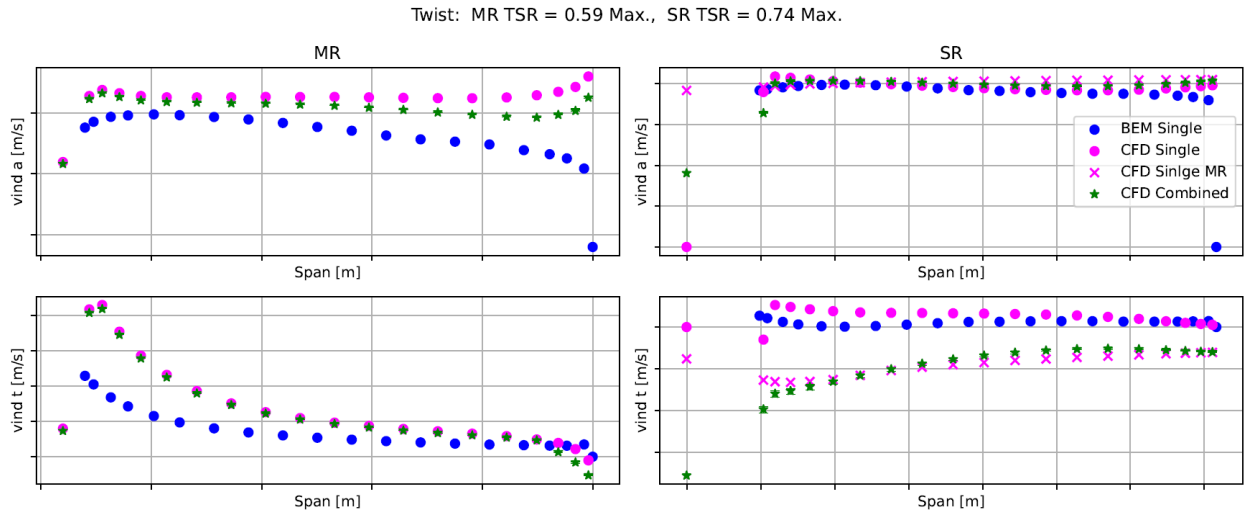

Figure 35. Combined-stage CFD – twist TSR C: spanwise-induced velocity distribution

7.1.3 Mid-Fidelity Model

After completing the high-fidelity cases, which provided valuable insight into the coupled flow dynamics around the secondary rotors, the NLR and EQOT teams discussed the most effective mid-fidelity modeling strategy and selected the FVW method (OLAF). The selection of this method was guided primarily by EQOT's desire to develop a model that was applicable across a wider range of geometries and operating conditions and not dependent on correction factors derived from CFD for a specific set of cases.

7.1.3.1 OLAF Parameter Tuning

The FVW model implemented in OpenFAST's AeroDyn module requires several parameters to be tuned: the wake and wing regularization factors, which set the radii of the vortex cores, as well as the eddy viscosity used in the core spreading methods. The number of wake panels is set as well, which determines the discretization of the wake. All other options were left to default, as currently recommended in the OLAF documentation (NLR, OpenFAST OLAF Documentation, 2025), except the method used to calculate

the regularization parameters (i.e., the "RegDeterMethod" parameter), which was set to 3. This is not the default setting but is the value recommended in the OLAF documentation. This method calculates the regularization parameters as a fraction of the blade spanwise discretization. To tune the wake and wing regularization factors and the eddy viscosity, a series of parameter sweeps were run. These consisted of varying the three parameters of interest over a relatively large range of possible values for a simulation of the main rotor alone at a single TSR. The parameter space was then narrowed by discarding combinations of parameters that gave poor agreement with CFD results, and the smaller set of parameters was used in simulations of the main rotor alone across a range of TSRs. The parameter space was further reduced, and this even smaller set of parameters was used in simulations of the secondary rotor alone across a range of TSRs. Finally, a single combination of parameters that gave the best agreement with CFD results across a range of TSRs for the main and secondary rotors simulated in isolation, was chosen for the combined simulations. Details of the process used for OLAF parameter tuning are described in Section 7.1.3.2 and 7.1.3.3.

7.1.3.2 Single-Stage Main Rotor

The largest parameter sweep was conducted for the main rotor operating at a single TSR in isolation. The inflow and rotation speeds were chosen to give a TSR corresponding to one of the cases simulated using CFD. Following guidance outlined in the OLAF documentation, the wing and wake regularization factors were allowed to range from 0.1 to 3.0 in increments of 0.1. The eddy viscosity was set to 1, 100, or 1000 for each set of wing and wake factors, resulting in 2700 unique combinations. For each combination of parameters, the time step, maximum simulation time, and number of wake panels was held constant. These were set according to best practices outlined in the OLAF documentation. The time step was set such that the rotor advanced 6 degrees between iterations. The maximum simulation time was set such that the wake could develop for a length of 4D downstream of the rotor. Only near-wake panels were used, as recommended, to improve accuracy. The results are shown in Figure 36, where the left column of plots shows the Cp error, the middle column shows the Ct error, and the right column shows the Cq error, as compared to CFD. Plots in the top row have an eddy viscosity of 1, plots in the middle row have an eddy viscosity of 100, and plots in the bottom row have an eddy viscosity of 1000. Within each plot, the *x* and *y* axes show the variations of the wake and wing regularization factors between 0.1 and 3.0. The color bar corresponds to the values of Cp, Ct, or Cq error. The significant variation of Cp, Ct, and Cq error with varying wing and wake factors illustrates the sensitivity of the simulation to these parameters. The relative similarity in plots within each column, however, indicates that the results are fairly insensitive to changes in the eddy viscosity. To narrow the parameter space, an eddy viscosity of 1000 was chosen, as the results displayed minimal sensitivity to this parameter and tended to give slightly better agreement with CFD than the results in the first and second rows. The parameter space was narrowed further by selecting only combinations of wing and wake factors that gave Cp, Ct, and Cq agreement within 10% of the CFD values. These are highlighted with red "x" markers in Figure 37.

After narrowing the parameter space from 2700 to 115 combinations, the main rotor was simulated again in isolation across a range of TSRs for the remaining 115 parameter sets. Again, the time step, maximum simulation time, and number of wake panels were set according to OLAF best practices. These parameters depend on the rotation speed of the rotor, which was changing for these simulations. The rotation speed giving the most conservative values of time step, simulation time, and number of wake panels was chosen, and these values were used for all rotation speeds to simplify the simulation setup. To further narrow the

parameter space, the resulting Cp, Ct, and Cq errors were calculated based on the CFD results at each TSR for each combination of wing and wake factors. The error was then averaged over all TSRs for each unique parameter set, as shown in Figure 38, where the size and color of the circles correspond to this average error. The blue squares denote which parameter combinations give agreement of the Cp, Ct, and Cq within 10% of the CFD results.

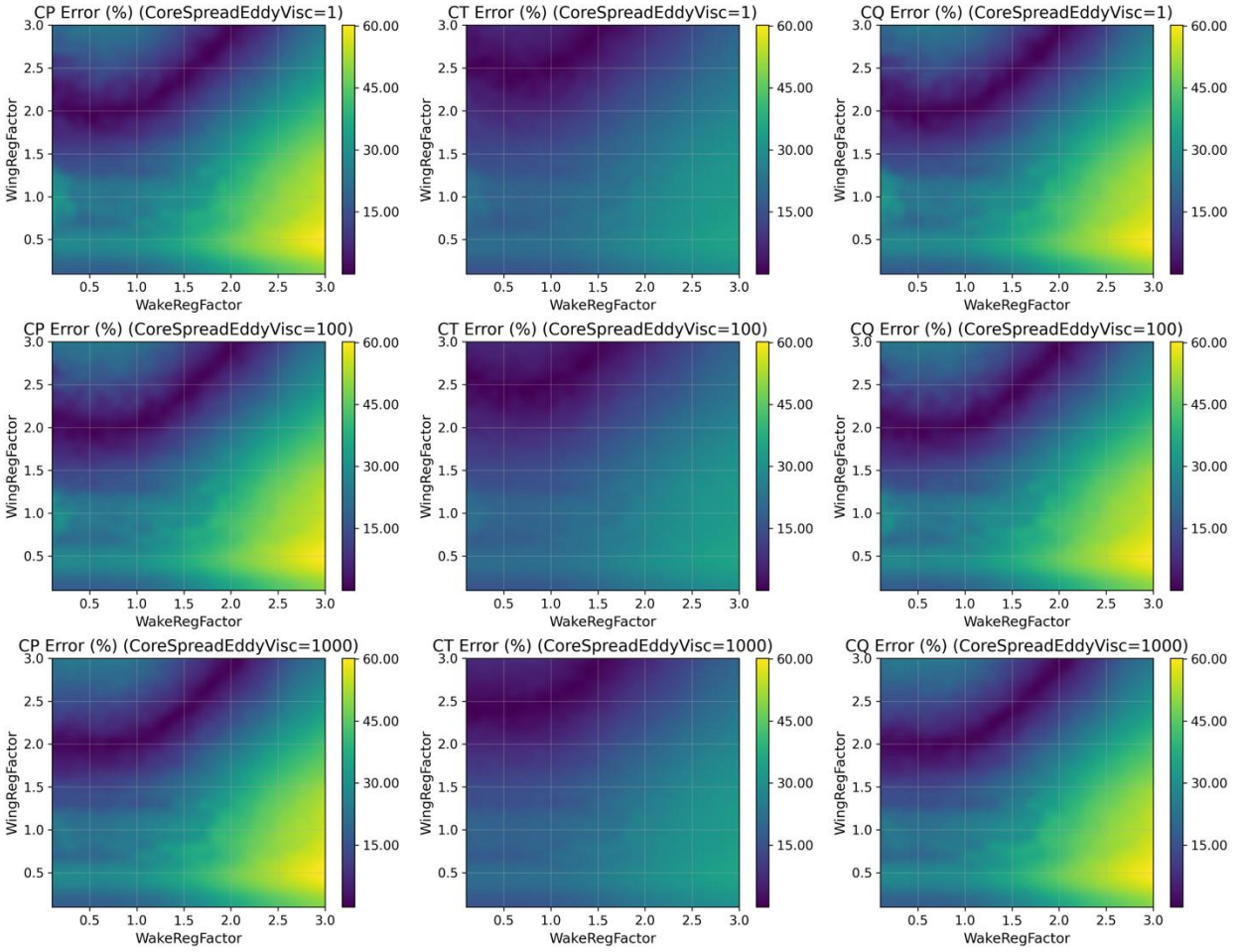

Figure 36. Power, thrust, and torque coefficient errors compared to CFD for the main rotor simulated in isolation using OLAF for the full range of wake, wing, and eddy viscosity parameters

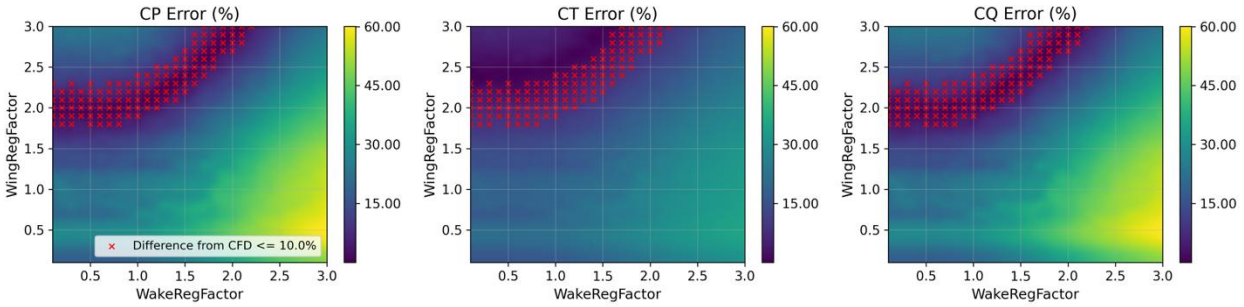

Figure 37. Combinations of wing and wake parameters that give 10% or less error between OLAF and CFD simulations of the main rotor operating in isolation at a single TSR are denoted by red "x" markers

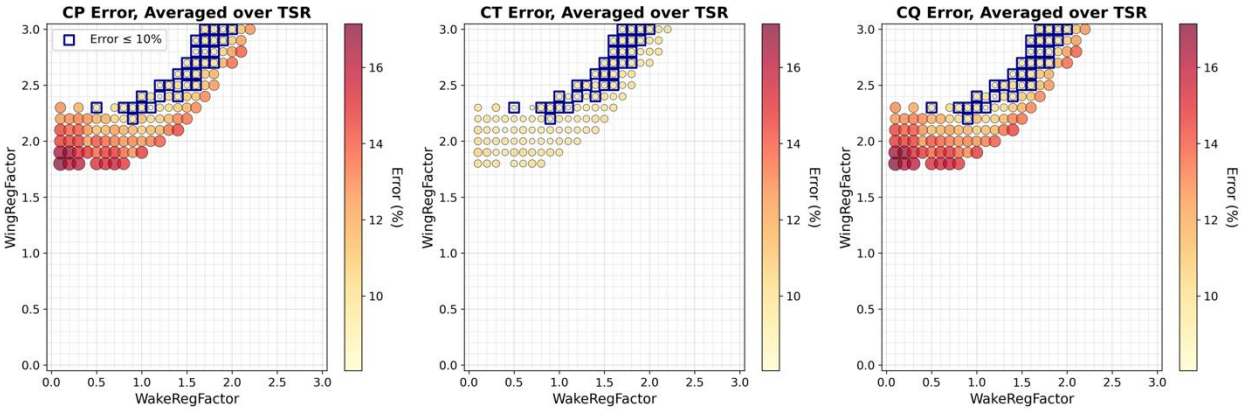

Figure 38. Power, thrust, and torque coefficient error from OLAF simulations, as compared to CFD, of the main rotor operating in isolation across a range of TSRs; for each combination of wing and wake factors, the error shown is averaged over the range of TSRs simulated

7.1.3.3 Single-Stage Secondary Rotor

The results shown in Figure 38 were used to further reduce the parameter space from 115 to 31 combinations, and these parameters were used to simulate the secondary rotor in isolation across a range of TSRs. The secondary rotor Cp, Cq, and Ct values were then compared to CFD results. To select the best single combination of parameters from the remaining 31, the Cp, Cq, and Ct error for both the main and secondary rotors was considered, as well as error in the blade loads along the span. Finally, a wake regularization factor of 1.2, a wing regularization factor of 2.4, and an eddy viscosity of 1000 were chosen for the combined-stage simulations. Comparisons of Cp and Ct for both the main and secondary rotors against CFD and BEM results are shown in Figure 39. It is interesting to note that the best-case tuned wake regularization factor results in a tip vortex core radius similar to that found in the single-stage main rotor CFD, as shown in Figure 15.

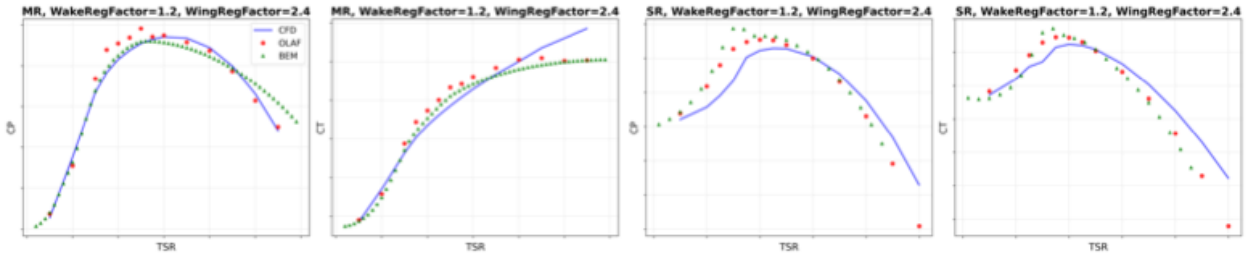

Figure 39. Power and thrust coefficients for the main (left two plots) and secondary (right two plots) rotors operating in isolation. Results from BEM, OLAF, and CFD are all shown; the OLAF results were generated using the final set of tuned parameters.

7.1.3.4 Combined Stage

After selecting a single combination of wing, wake, and eddy viscosity parameters that gave the best agreement with CFD for the main and secondary rotors simulated in isolation, these parameters were used in a combined-stage simulation of the single main rotor and two secondary rotors. Because the main and secondary rotors have significantly different length and time scales, setting the time step, simulation time, and number of wake panels for a combined-stage simulation is less straightforward than for a single rotor simulation. An attempt was made to balance the refinement needed for the small length and time scales of the secondary rotor with an efficient computational time. Figure 40 and Figure 41 show blade loads from a combined-stage simulation along the span of a single blade for both the main and secondary rotors using different values for the time step and number of wake panels. Results for different modeling approaches are shown, with the combined-stage OLAF plotted in yellow. Figure 40 is for a larger time step and smaller number of wake panels (i.e., more tuned for the dimensions of the main rotor), and Figure 41 is for a smaller time step and larger number of wake panels (i.e., more tuned for the dimensions of the secondary rotor). Understandably, the blade loads are more accurate for the main rotor in Figure 40 and for the secondary rotor in Figure 41. Unfortunately, within the scope of this project, we were not able to identify a combination of time step and wake panels that gave acceptable accuracy compared to the combined-stage CFD results. There are several additional parameter changes that could be explored, as well as modifications that could be implemented within OLAF, to improve these results. Options for improving the combined-stage OLAF simulations will be the subject of potential future work.

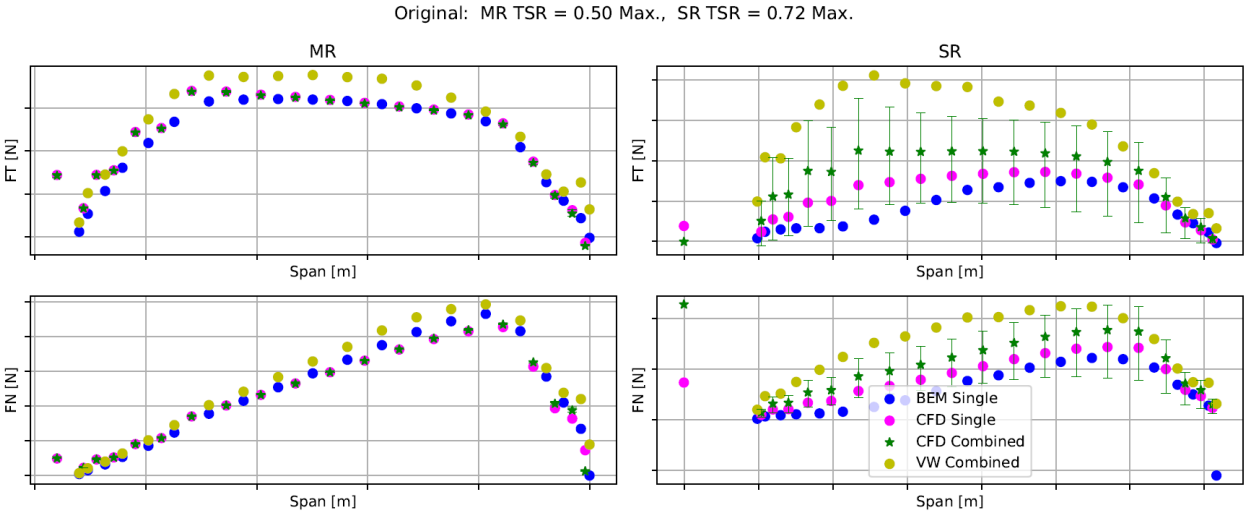

Figure 40. Combined-stage OLAF: spanwise blade load distribution using a time step and number of wake panels better suited for the main rotor

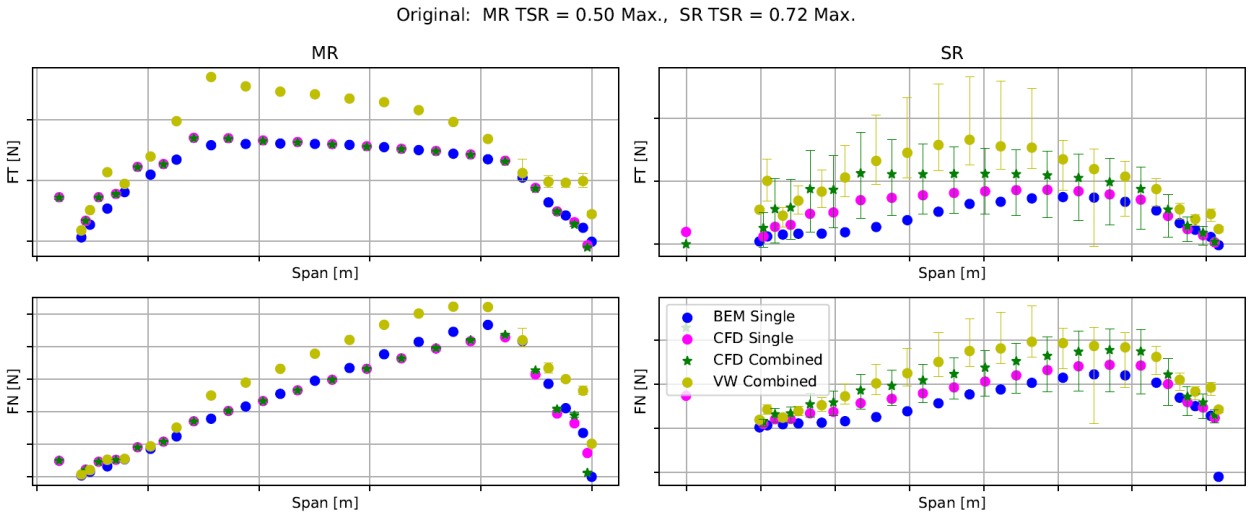

Figure 41. Combined-stage OLAF: spanwise blade load distribution using a time step and number of wake panels better suited for the secondary rotor

7.1.4 BEM with Custom Inflow

Given that satisfactory accuracy was not achieved with a combined-stage OLAF simulation, an alternative mid-fidelity approach was also tested. This approach involved one-way coupling of the rotor interactions by modeling the secondary rotor using single-stage BEM, with a custom inflow based on the simulation of a single-stage main rotor. For this approach, the flow is sampled behind the trailing edge of the main rotor blade tip, for a plane matching the location of the secondary rotor if it was present. Both CFD and OLAF can provide a prediction of the flow field in this location. Figure 42 and Figure 43 show the sampled flow from single-stage CFD and OLAF, respectively. All three velocity components are shown in the reference frame of the secondary rotor. This includes the apparent velocity from the main rotor rotation, which

appears as a vertical gradient in the “u” plot on the left of each figure. Note that the color scales are the same for the corresponding components between Figure 42 and Figure 43.

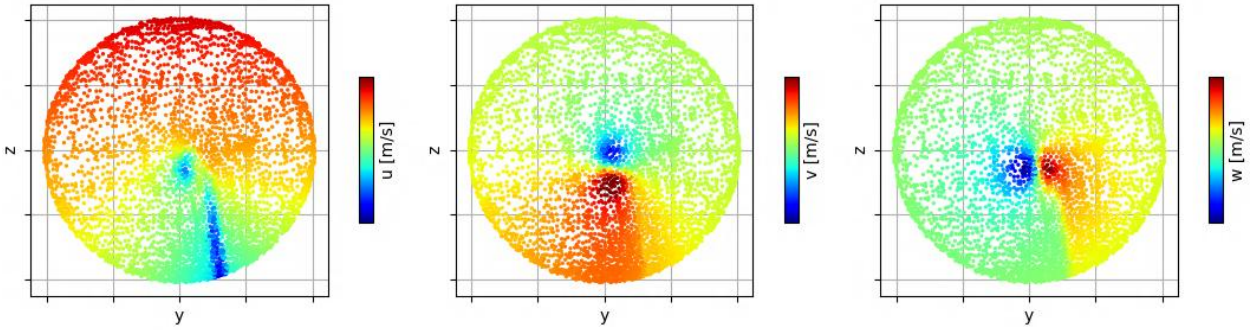

Figure 42. Secondary rotor plane inflow measured in main rotor single-stage CFD

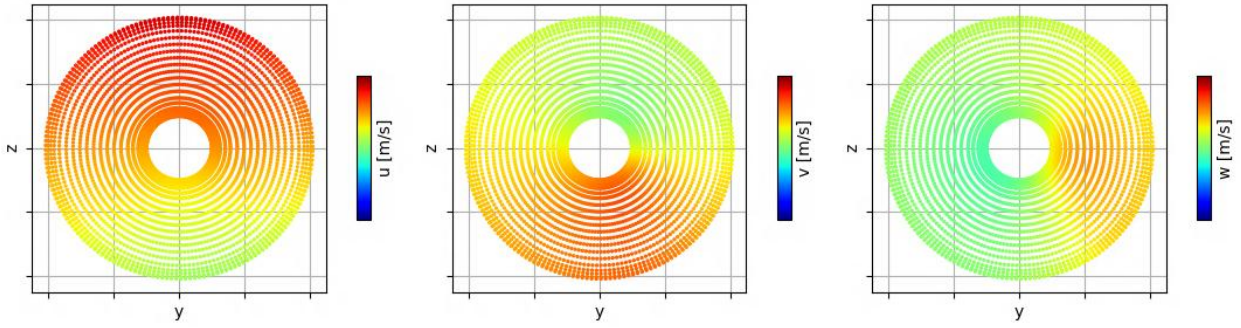

Figure 43. Secondary rotor plane inflow measured in main rotor single-stage OLAF

The CFD flow field has more detailed flow captured. In the u direction, the CFD shows a sharp drop in velocity along a close-to-vertical line from the bottom to the center of the secondary rotor plane. This is from the viscous wake behind the main rotor trailing edge, which has no way to be captured in a vortex model. This deficit is important to capture for blade fatigue, drivetrain loading, and controller stability. However, the rotational flow from the main rotor tip vortex, shown in the v and w plots, is relatively well captured by the mid-fidelity model. While the CFD predicted flow rotation is not a perfect circular potential flow vortex, with some sharper changes in speed, the general magnitudes and gradients match the OLAF predictions well.

Figure 44 and Figure 45 show the blade load distribution comparison, also including predictions using this custom inflow approach. Figure 44 uses the inflow from CFD, and Figure 45 uses the inflow from OLAF. The key comparison here, which demonstrates the one-way rotor interaction, is the difference between the combined-stage (green) and single-stage (pink) CFD compared to the difference between the custom inflow (red) and single-stage (blue) BEM. Using both the CFD and OLAF inflow, the same general change in mean tangential and normal force is captured, and for the same spanwise positions, indicating that capturing the one-way coupled interaction does a good job of capturing the total interaction. The variability in the predicted loads changes considerably between the CFD and OLAF inflow. The minimum-to-maximum range is largely underpredicted with the OLAF inflow, as compared to the full combined-stage CFD, likely due to the missing viscous wake in the secondary rotor u direction. The minimum-to-

maximum range when using the CFD inflow, however, is overpredicted compared to the full combined-stage CFD. This is likely due to some missing two-way flow coupling, where the presence of the secondary rotor changes what the main rotor tip trailing edge viscous wake looks like. Because it generally does a good job of capturing the impact of the secondary rotor apparent flow rotation, that this method can be useful for geometry refinement of the secondary rotor.

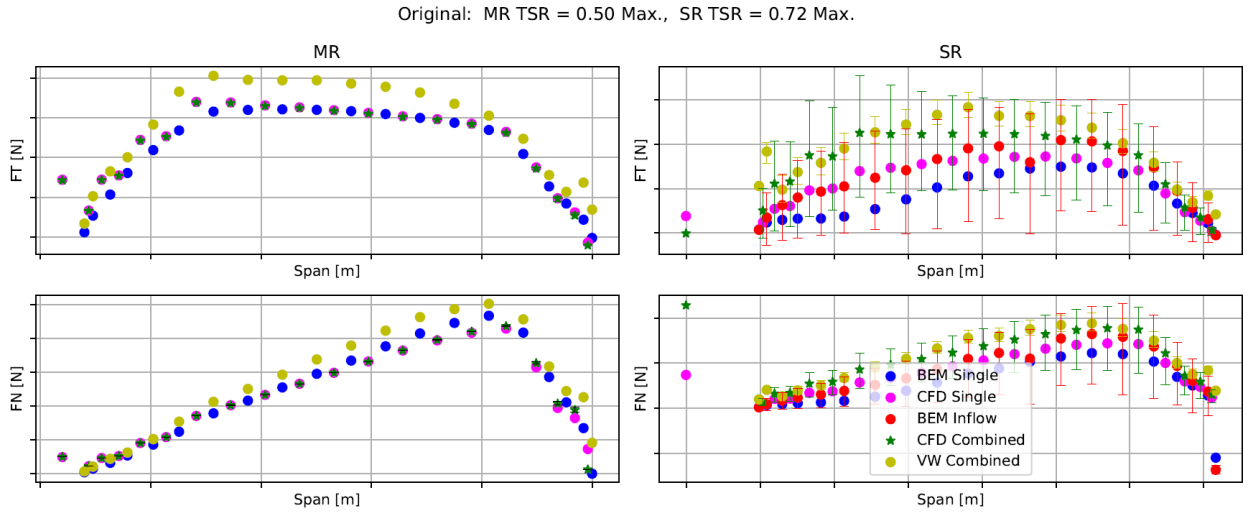

Figure 44. Spanwise blade load distribution including secondary rotor predictions from single-stage BEM with custom inflow from main rotor single-stage CFD (VW combined OLAF results shown with intermediate parameters)

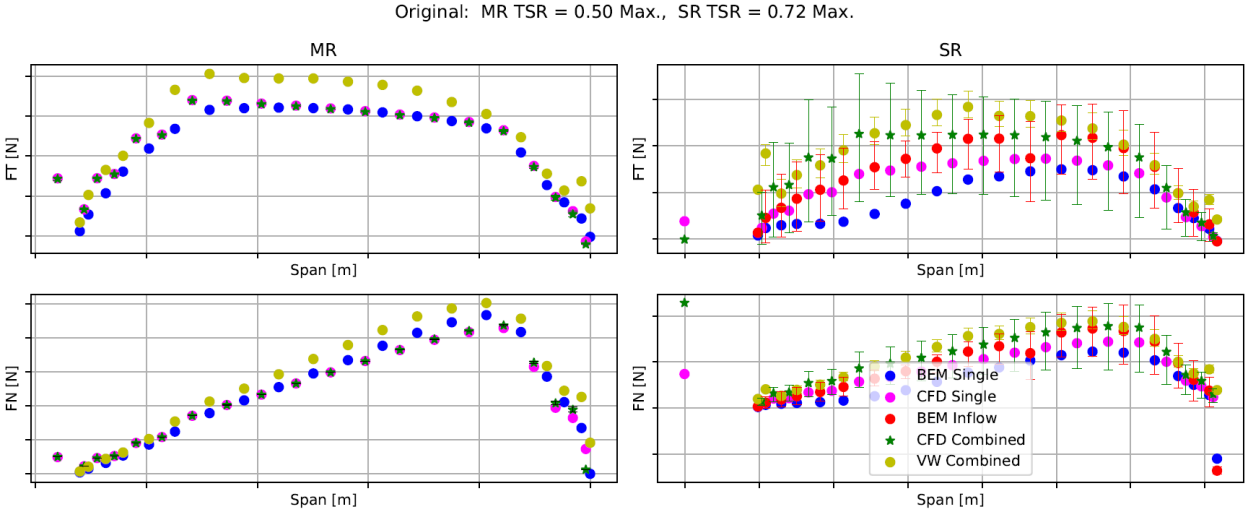

Figure 45. Spanwise blade load distribution including secondary rotor predictions from single-stage BEM with custom inflow from main rotor single-stage OLAF (VW combined OLAF results shown with intermediate parameters)

7.2 Lesson Learned and Test Plan Deviation

The key lessons learned pertain to the importance of certain flow interactions between the stages of a two-stage turbine and the ability of different fluids models to capture them. To enable better exploration of the interaction between the main rotor tip vortex and the secondary rotor rotation, a minor deviation

was made from the original plan of simulating three different tip turbine foil shapes. Rather than three different foil shapes, two foil shapes were simulated (the original geometry as provided by EQOT and a geometry with an altered twist). In addition, the original geometry was simulated with a reverse rotation direction.

The original plans included the use of the OpenFAST structural module ElastoDyn, as well as the ServoDyn and StC modules, to determine and control the motion of the individual rotors in the mid-fidelity model and to impose forces as needed. The focus of this work was understanding the hydrodynamic interactions; therefore, it was beneficial for the motions to exactly match when comparing between fidelity levels so that the differences would be fully attributed to the fluids model and not to different rotation speeds. It was decided to use prescribed constant rotation speeds in the mid-fidelity modeling to allow direct comparisons to the CFD results. This was done without the need for ElastoDyn or any OpenFAST modules other than AeroDyn. A separate Python wrapper was set up to enable the use of a multibody code to calculate the rigid-body rotations. However, this wrapper was not sufficiently developed for use in the production load cases for this project since it was not needed. Therefore, it would not serve as a complete, open-source example and was not released publicly.

The original method for determining whether to select BEM or FVW for the mid-fidelity model was based on analyzing correction factors derived from CFD for different turbine geometries. If these correction factors varied significantly between geometries, indicating sensitivity to changes in the turbine design, the intention was to choose the FVW method. Otherwise, we would assume that the same corrections could be used for geometries that were not explicitly simulated in CFD, and a BEM method could be used. Ultimately, the initial choice of using the FVW method came down to a desire to model the system fully in a mid-fidelity code without the need for input from CFD simulations. CFD is challenging for EQOT to complete internally, and the goal was to establish a mid-fidelity modeling method that EQOT could use independently after completion of the TEAMER project. Achieving an adequate balance of accuracy and computational time with the FVW approach proved challenging, as described in Section 7.1.3.4, which motivated the method described in Section 7.1.4 that uses a single-stage secondary rotor BEM simulation with a custom inflow. Due to the challenges establishing a workable mid-fidelity method, the full set of planned design load cases was not completed. Instead, comparisons between CFD and the different mid-fidelity approaches were made for a smaller set of operating conditions (i.e., Figure 44 and Figure 45).

8 Conclusions and Recommendations

Hydrodynamic interactions of a two-stage rotor were identified through high-fidelity CFD modeling. This highlighted the impact of the main rotor tip vortex and wake on the secondary rotor apparent inflow. This results in a relative flow rotation and sharp deficit, that change the optimal secondary rotor rotation speed and adds unsteadiness to the blade loading respectively. Multiple mid-fidelity approaches were evaluated for their ability to capture these effects. As shown in Figure 17, a simple approximation of the combined-stage performance based on single-stage BEM provides a reasonable rough prediction, especially near the peak TSR values, with some larger discrepancy at higher TSRs. Predicting the combined-stage performance based on single-stage CFD data improves this prediction across the TSR range. Although the combined-stage modeling in OLAF was not successful in this stage of the project, it showed promise as a mid-fidelity

method, assuming the parameters can be tuned to account for the significant differences in time and length scales between the main and secondary rotors. This may be addressed through code changes in future work. A significant finding from the OLAF work was the agreement between the vortex core radius values found independently via a parameter space search and via CFD. The technique of using single-stage secondary rotor BEM, with a custom inflow taken from single-stage main rotor CFD or OLAF, provides an efficient method to capture one-way coupled flow interactions. This method provided generally good predictions of the impact of the flow rotation on the secondary rotor but struggled to accurately predict the peaks of the unsteady load progression. Future work could include some superposition of a tuned main rotor trailing edge viscous wake into the custom inflow to better predict this interaction.

The next step is to look at the full semi-floating system. A number of additions are needed, including:

- Six-degree-of-freedom platform motions
- Non-fixed rotor speeds
- Moorings
- Non-uniform inflow

This full system modeling will be the subject of future proposals.

9 REFERENCES

https://equinoxoceanturbines.com/

Mendes, R., Macias, M., Oliveira, T., & Brasil, A. (2021). A Computational Fluid Dynamics Investigation on the Axial Induction Factor of a Small Horizontal Axis Wind Turbine. *Journal of Energy Resources Technology*. doi:https://doi.org/10.1115/1.4048081

MIT. (2025). *XFOIL*. Retrieved from https://web.mit.edu/drela/Public/web/xfoil/

NLR. (2025). *GitHub AirfoilPreppy*. Retrieved from https://github.com/NLRWindSystems/AirfoilPreppy

NLR. (2025). *GitHub Multibody for Everybody*. Retrieved from GitHub: https://github.com/Project-SEA-Stack/MATLAB_Multibody_for_Everybody

NLR. (2025). *GitHub OpenFAST*. Retrieved from https://github.com/OpenFAST/openfast

NLR. (2025). *OpenFAST OLAF Documentation*. Retrieved from readthedocs: https://openfast.readthedocs.io/en/dev/source/user/aerodyn-olaf/index.html

10 ACKNOWLEDGEMENTS

A portion of this research was performed using computational resources sponsored by the U.S. Department of Energy's Office of Critical Minerals and Energy Innovation and located at the National Laboratory of the Rockies.

This work was authored by the National Laboratory of the Rockies for the U.S. Department of Energy (DOE), operated under Contract No. DE-AC36-08GO28308. Funding provided by U.S. Department of Energy Office of Critical Minerals and Energy Innovation Water Power Technologies Office. The views expressed in the article do not necessarily represent the views of the DOE or the U.S. Government. The U.S. Government retains and the publisher, by accepting the article for publication, acknowledges that the U.S. Government retains a nonexclusive, paid-up, irrevocable, worldwide license to publish or reproduce the published form of this work, or allow others to do so, for U.S. Government purposes.